Supplementary Material to "Bedload transport's scaling behavior: what if Bagnold was right?"

Christophe ANCEY[1] and Alain RECKING[2]

[1] *École Polytechnique Fédérale de Lausanne, Station 18, 1015 Lausanne, Switzerland (christophe.ancey@epfl.ch)*

[2] *University of Grenoble Alpes, INRAE, CNRS, IRD, Grenoble INP, IGE, 38000 Grenoble, France (alain.recking@inrae.fr)*

Contents

The Supplementary Material provides further information about Bagnold's model calibration and the sources of all the field data used in the article. Here are the contents:

- In Sec. S1, we explain how the dynamic friction factor μ, efficiency factor e_b, and Darcy-Weisbach factor f were calibrated. If the bedload transport rate cannot be entirely calculated using conservation principles in a simple manner, the only way to close the bedload transport equation (8) involves using empirical closure equations to determine how Bagnold's dynamic friction factor $\mu = \tan\alpha$ and efficiency factor e_b depend on flow parameters. We also synthesize the various efforts made for evaluating flow resistance in clear water flows over plane beds, and when bedforms and/or sediment transport increase energy dissipation.

- Section S2 gives more detail about the empirical flow resistance equations used in Section S1.

- Section S3 provides additional explanations about the notation used in Table 6.

- Section S4 contains additional plots that support some statements in the review article or supplement the analysis of field data. Section S4.1 shows that the scaling suggested by Parker et al. (2011) and Ferguson (2012) is a relevant alternative to the scaling $\Phi = 4M$ referred to as Bagnold's scaling in our review article. Gravel-bed rivers usually involve wide grain size distributions, and the question arises as to how sediment gradation d_{84}/d_{50} influences bedload transport rates, and in particular whether the coarse grain diameter d_{84} is more representative of the bed state than the median diameter d_{50} (see Sec. S4.2). Section S4.3 explores a related issue: instead of using the dimensionless variables Φ and τ^*, we consider the scaled bedload transport rate and stress W^* and φ proposed by Parker et al. (1982). In Sec. S4.4, we show a close-up view of Fig. 3(a). Section S4.5 shows that for 17 streams, Bagnold's master equation performs well at predicting transport rates. Section S4.6 provides further information about the e_b variations with the Shield stress τ^*. Section S4.7 shows the n values in the power law $\Phi \propto \tau^{*n}$ determined by two-phase numerical models in the (R, τ^*) diagram.

- Section S5 describes the sources of all the data used for relating bedload transport rates to flow conditions for gravel-bed and sand-bed rivers in Fig. 5.

- Section S6 explains how to use the scripts and data available from the Zenodo depository doi.org/10.5281/zenodo.7746863.

S1 Model calibration

S1.1 Calibration of the dynamic friction factor μ

For the friction coefficient μ, Bagnold (1956) found a dependence on the dimensionless number that came to bear this name:

$$G^2 = \frac{\varrho_s \tau_b d^2}{14\eta^2} = \frac{\varrho_s}{\varrho}\frac{\tau^*}{14}R^2, \tag{S1}$$

where $\eta = \varrho\nu$ is the water's dynamic viscosity [kg·m^{-1}·s^{-1}].

Bagnold found that for $G^2 \leq 100$, $\mu = \tan\alpha \to 0.75$, whereas for $G^2 \geq 8000$, $\tan\alpha \to 0.375$. Figure S1 shows the μ variation with G^2 that Bagnold (1966) obtained. In the following, the dependence of the friction angle $\tan\alpha$ on the dimensionless number G is approximated by the empirical equation:

$$\mu = \tan\alpha = \tan\alpha_{max} - \tan\alpha_{min}\tanh\frac{G^{1.8}}{1000}, \tag{S2}$$

with $\tan\alpha_{max} = 0.75$ and $\tan\alpha_{max} = 0.375$.

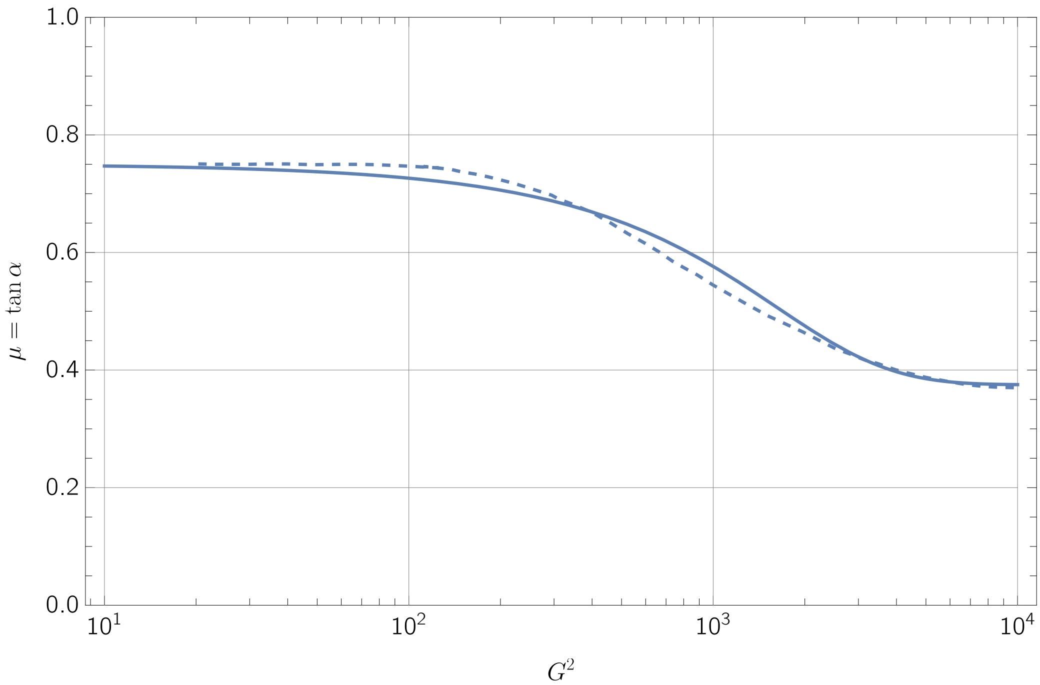

Figure S1. Reproduction of Bagnold's diagram $\tan\alpha = f(G^2)$, scanned from Bagnold (1966) (solid line). The dashed curve shows Bagnold's result, while the solid line shows the approximation (S2).

S1.2 Calibration of the efficiency factor e_b

Based on heuristic considerations and his earlier experimental work on granular suspensions, Bagnold (1966) stated that the efficiency factor's upper bound was 0.15. Apart from this upper bound, Bagnold (1966) did not provide much information about the e_b dependence. In his 1973 paper, Bagnold calculated the efficiency factor e_b for saltating particles (for flows in a transitional regime) as a function of the shear velocity, flow depth, and mean velocity, and he stated that at the highest transport rates, e_b should tend towards a constant value that remained lower than unity for unsuspended particles. In 1977, he abandoned the idea of calculating the efficiency factor and instead used empirical evidence to provide the following scaling law:

$$e_b = 1.6\sqrt{\frac{\omega - \omega_c}{\omega_c}}\left(\frac{h}{d}\right)^{-2/3}, \tag{S3}$$

where ω_c denotes the threshold stream power (related to sediment's incipient motion) [W·m^{-2}]. In 1980, he corrected this equation and proposed a new scaling:

$$e_b \propto (\omega - \omega_c)^{1/2} d^{-1/2} h^{-2/3}. \tag{S4}$$

Studying two gravel-streams in the Pennines, Carling (1989) found a slightly different correlation: $e_b = 0.2(h/d)^{-0.4}$. Compiling field and laboratory data, Gomez (2022) noted a significant variability in the efficiency factor e_b (up to four orders of magnitude for a given median diameter). He also found that e_b was bounded between an upper limit ($e_{b,max} = 0.011d^{-0.51}$) and a lower limit ($e_{b,min} = 2.34\times10^{-7}d^{-2}$) (Gomez, 2006, 2022). His upper limit is consistent with Bagnold's equation (S4) for the dependence of e_b on d.

Although Bagnold (1980, 1986) reported a good agreement between this scaling and bedload transport rate data (from laboratory flumes and field surveys), Martin and Church (2000) noted that Bagnold selected just a few datasets from among the many available at that time, and discarded others without providing any justification for doing so. They also found an inconsistency in the scaling, which led them to reconsider the dependence of e_b on flow parameters. Proceeding by trial and error, they found that the scaling of

$$e_b \propto (\omega - \omega_c)^{1/2} d^{1/4} h^{-1} \varrho^{-1/2} g^{-9/4} \tag{S5}$$

provided the best fit with the data. As dimensionless forms are often preferable to monomial products (with no clear physical interpretation), we recast Martin and Church's suggestion in the form of a product of the following dimensionless groups: the scaled stream power $\Omega = \omega/(\nu g \varrho)$, the particle Reynolds number R, the relative submergence $\xi = h/d$, and the density ratio s. Equation (S5) then reads,

$$e_b \propto \Omega^{1/2} \xi^{-1} s^{-1/4} R^{-1/2}, \tag{S6}$$

which implies that the dimensionless bedload transport rate varies as $\Omega^{3/2}$:

$$\Phi \propto \Omega^{3/2} \xi^{-1} s^{-5/4} R^{-3/2}. \tag{S7}$$

To further test this scaling, we defined the dimensionless number $\Pi = \Omega^{a_1} \xi^{a_2} R^{a_3} s^{a_4}$, where the exponents a_1 to a_4 were free parameters to be adjusted from data. We used the data recapped in Table S1 to set these exponents using a Markov chain Monte Carlo algorithm. We found $a_1 = 0.50 \pm 0.04$, $a_2 = -0.49 \pm 0.08$, $a_3 = -0.66 \pm 0.05$, and $a_4 = -0.83 \pm 0.08$. By setting, $a_1 = 1/2$, $a_2 = -1/2$, $a_3 = -2/3$, and $a_4 = -4/5$, we found that $e_b \propto \Pi$. We eventually ended up with the following scalings:

$$\begin{aligned} e_b \propto \Pi &= \Omega^{1/2} \xi^{-1/2} R^{-2/3} s^{-4/5} \text{ and} \\ \Phi \propto M &= \Omega^{3/2} \xi^{-1/2} R^{-5/3} s^{-9/5}, \end{aligned} \tag{S8}$$

which performs slightly better than Eq. (S6) for the dataset used here—the coefficient of determination and the Bayesian information criterion were 0.61 and 1368, respectively, for Eq. (S8), whereas they were 0.56 and 1416 for Eq. (S6). The dimensionless number $M = \Omega^{3/2} \xi^{-1/2} R^{-5/3} s^{-9/5}$ has been labeled in reference to Yvonne Martin's contribution. As it was obtained by statistical adjustment, it has no special physical meaning.

As Fig. S2 shows, our updated Martin and Church's scaling (S8) roughly captures the experimental estimates of the efficiency factor e_b. We will see below that this agreement

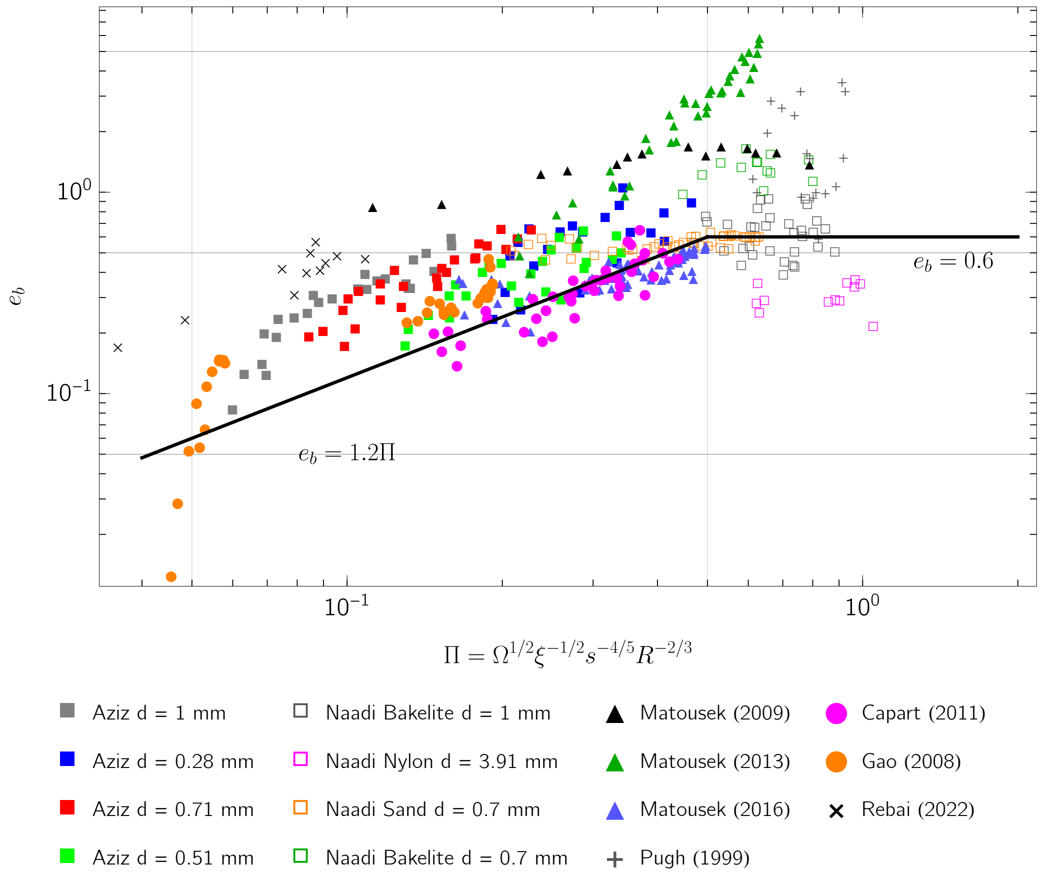

Figure S2. Variation in the efficiency factor e_b with the dimensionless number $\Pi = \Omega^{1/2}\xi^{-1/2}s^{-4/5}R^{-2/3}$. The solid line shows the trend of $e_b = 1.2\Pi$ for $\Pi < 0.5$ and the trend of $e_b = 0.6$ for $\Pi \geq 0.5$. The experimental data come from the sources listed in Table S1.

Table S1. Experimental data considered in Figs S2 and S3. We report the type of experimental facility (flume with a free-surface flow or pressurized rectangular/cylindrical pipes), the ratio of the settling velocity w_s to the friction velocity u_*, the median particle diameter d_{50}, its density ratio $s = \varrho_s/\varrho - 1$, the range of flume/pipe slopes, and the range of Shields numbers. Wilson (1966) provided only partial information about his experiments (the data used in Fig. S2 were obtained by digitizing his Figure 2).

Authors	Device	w_s/u_*	d_{50} (mm)	s	i (%)	τ^*
Wilson (1966)	rect. pipe	1.2–4.8	0.7	1.67	–	0.5–7.3
Aziz and Scott (1989)	flume	0.5–4.6	0.3–1	1.65	3–10	0.1–0.9
Nnadi and Wilson (1992)	rect. pipe	0.4–1.4	0.7–4	0.14–1.67	1.7–7	0.1–0.9
Pugh and Wilson (1999)	cyl. pipe	0.1–0.7	0.3–1	0.53–1.65	2–12	2–18
Gao (2008)	flume	1.2–6.9	1–7	1.65	2.5–3.3	0.07–1.2
Capart and Fraccarollo (2011)	flume	1.0–2.6	3.35	0.51	1–8	0.4–2.5
Matoušek (2009)	cyl. pipe	0.1–0.8	0.37	1.65	2–16	0.7–23
Matoušek et al. (2013)	rect. pipe	0.1–0.5	0.18	0.45	1–6.5	0.5–6
Matoušek et al. (2016)	flume	1.0–2.8	0.32	0.36	0.5–6	0.4–22
Rebai et al. (2022)	flume	1.4–3.4	3.6–6.4	0.4	1.2–5.9	0.3–1.3

is even more obvious when working with bedload transport rates instead of e_b (see § 2.8.3). In Fig. S2, we used data from various laboratory facilities and whose origins are reported in Table S1. Whereas these data support Bagnold's idea that bedload transport rates scale with stream power, we found no strong correlation between the efficiency factor e_b and the dimensionless number Π. One possible empirical law could be the following:

$$e_b = 1.2\Pi \text{ for } \Pi < 0.5 \text{ and } e_b = 0.6 \text{ for } \Pi \geq 0.5. \tag{S9}$$

However, not all the data fall close to this empirical relationship.

Expressing the efficiency factor e_b as a function of Π raises two issues. First, the number Π has no clear physical meaning. Second, Bagnold used the dimensionless shear stress τ^* in his flow regime classification, and the stream power ω as the driving variable in his bedload transport rate equation. It may be more efficient to seek a dependence of the efficiency factor e_b on τ^*. We used the data recapped in Table S1 and estimated the efficiency factor by using Eq. (4), where the friction factor μ was estimated using Bagnold's equation (S2) and the stream power was computed as $\omega = \varrho g q i = \tau_b \bar{u}$. With these assumptions, we can estimate e_b from laboratory data: $e_b = q_s \mu \cos\theta g \Delta\varrho/\omega$. When plotting the efficiency factor e_b with the Shields number τ^* (see Fig. S3), we find two experimental trends that are consistent with Bagnold's partitioning into bedload transport regimes:

- For the transitional regime ($\tau^* \leq \tau_x^*$ with $\tau_x^* \sim 0.5$), the efficiency factor e_b increases with increasing Shields numbers τ^*:

$$e_b = 2\tau^{*3/2}. \tag{S10}$$

- For the sheet-flow regime ($\tau^* > \tau_x^*$), the efficiency factor e_b shows weak dependence on τ^*: $e_b = 0.4\tau^{*1/5}$. As a first approximation, we can consider that it reaches a constant value, but there is no unique plateau value. The asymptotic value ranges from 0.2 to 1. Not all data follow this trend. When sediment is made up of light, fine particles (see the data obtained by Matoušek et al. (2013) and Pugh and Wilson (1999) in Fig. S3), turbulence maintains those particles in suspension and the efficiency factor does not tend to a constant value.

S1.3 Calibration of Flow Resistance f

The last parameter involved in Bagnold's bedload transport rate equation (8) is the Darcy–Weisbach friction coefficient f, which represents resistance to flow. This coefficient f depends on dimensionless numbers such as the Reynolds and Froude numbers ($\mathrm{Re} = \bar{u}h/\nu$ and $\mathrm{Fr} = \bar{u}/\sqrt{gh}$, respectively) and on the relative submergence ξ (defined as $\xi = h/k_s$, where k_s is the bed roughness size [m]): $f = f(\mathrm{Re}, \mathrm{Fr}, \xi, \ldots)$ (Rouse, 1965; Colosimo et al., 1988). Keulegan (1938) showed that for sufficiently deep flows over fixed-plane gravel beds, the velocity profile is consistent with the logarithmic profile provided by Prandtl's parametrization of the turbulent viscosity for turbulent flows near a solid boundary, and thus the depth-averaged velocity $\bar{u}$ can be expressed as a function of the friction velocity u_* and relative submergence ξ:

$$\frac{\bar{u}}{u_*} = 6.25 + 5.75 \log \frac{h}{k_s}. \tag{S11}$$

This shows that the friction factor depends on relative submergence alone:

$$f = 8\left(\frac{u_*}{\bar{u}}\right)^2 = 8\left(6.25 + 5.75 \log \frac{h}{k_s}\right)^{-2} = \left(2.03 \log \frac{12.2h}{k_s}\right)^{-2}. \tag{S12}$$

For shallow flows (typically when $\xi < 10$), it becomes more difficult to define the level at which the velocity drops to zero (Nikora et al., 2001)—the level that serves to locate the

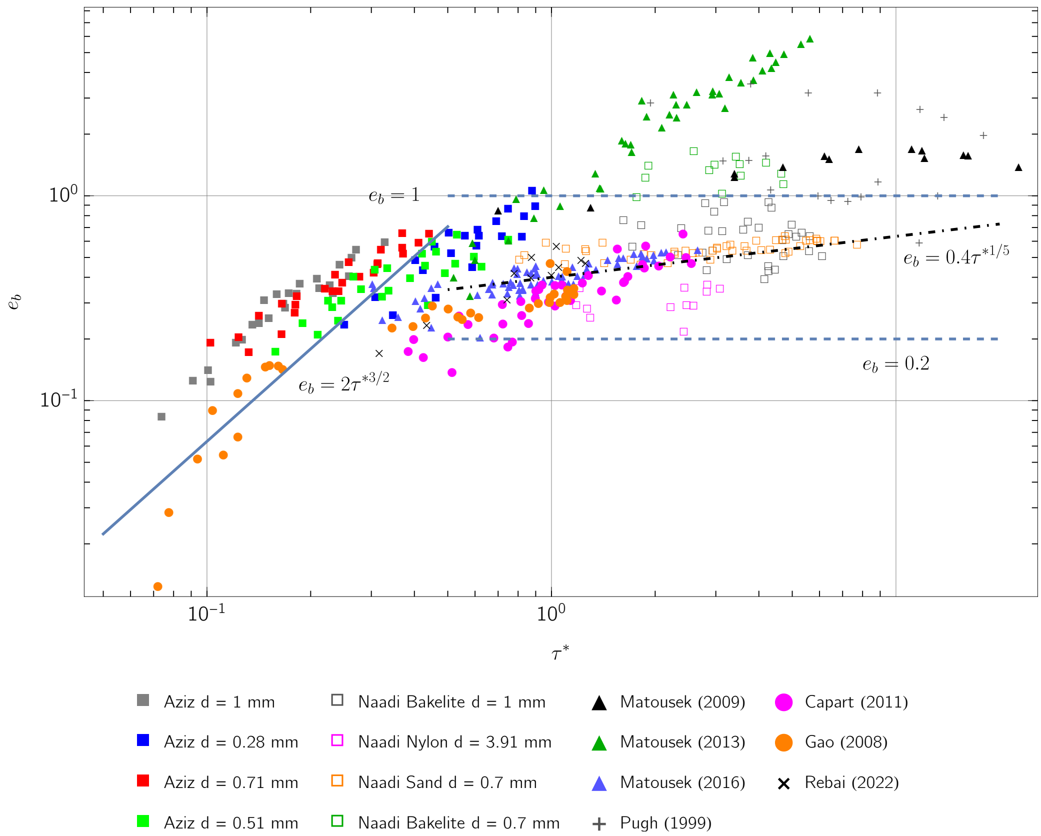

Figure S3. Variation in the efficiency factor e_b, with the Shields number τ^*, for the pipe data coming from the sources recapped in Table S1. The efficiency factor e_b was computed from experimental data by using Eq. (4): $e_b = q_s \mu \cos\theta g \Delta_p \varrho/\omega$. The solid line shows the empirical trend (S10). The dashed horizontal lines represent the upper and lower ranges within which the asymptotic efficiency factor lies.

stream/bed interface. Furthermore, when the instantaneous velocity field shows significant time and space variations, especially near the bed, Prandtl's model is no longer valid and must be replaced with more sophisticated parameterizations of wall turbulence (Nikora et al., 2004, 2007; Manes et al., 2007; Lamb et al., 2017; Nikora et al., 2019; Rousseau and Ancey, 2022; Deal, 2022). To avoid using refined parametrization, some authors have proposed correcting factors. For instance, Cao (1985) extended Keulegan's equation (S11) to low submergence by using a multiplicative factor dependent on the dimensionless number Y:

$$\sqrt{\frac{8}{f}} = \frac{\bar{u}}{u_*} = \left(6.25 + 5.75 \log \frac{h}{k_s}\right)\left(1 - \mathrm{e}^{-Y}\right). \tag{S13}$$

When Y is dependent on the relative submergence based on the median diameter d_{50} (the notation d_x refers to the quantile of particle diameters such that $x\%$ of the grains on the bed surface are finer than d_x),

$$Y = a\left(\frac{h}{d_{50}}\right)^b, \text{ where } a = 1.053 \text{ and } b = 0.255, \tag{S14}$$

but when it is dependent on the relative submergence and Froude number,

$$Y = a\left(\frac{h}{d_{50}}\right)^b \mathrm{Fr}^c, \text{ where } a = 0.834,\ b = 0.318, \text{ and } c = 0.779. \tag{S15}$$

Recking et al. (2008b) considered that under low submergence conditions, bed roughness was increased by a factor $\alpha_{rl} = 4\xi^{-0.43}$ (subject to $1 \leq \alpha_{rl} \leq 4$), rewriting Keulegan's equation (S11) in the form:

$$\sqrt{\frac{8}{f}} = \frac{\bar{u}}{u_*} = 6.25 + 5.75 \log \frac{h}{\alpha_{rl} k_s}. \tag{S16}$$

Recking et al. (2008b) also recommended using the characteristic diameter d_{84}, corresponding to the coarsest grain fraction, but they also mentioned that the median diameter d_{50} worked equally well. There is no consensus in the literature about the optimal value of the bed roughness size k_s: for gravel-bed rivers, $k_s = 2d_{90}$ (Kamphuis, 1974), $k_s = 3.5d_{84}$ (Hey, 1979), $k_s = 3d_{84}$ (Pitlick, 1992), $k_s = 5.9d_{50}$ (Millar, 1999), or $k_s = 2.4d_{90}$ (López and Barragán, 2008). None of these expressions provides better accuracy in velocity profile predictions (López and Barragán, 2008). According to Aberle and Smart (2003), a better way of defining the roughness size k_s is to scan the bed surface at the grain scale and then define k_s as the standard deviation of the detrended bed surface.

Figure S4 shows the f variation with relative submergence in the absence of sediment transport for plane gravel beds made of well-sorted gravel (with a gradation coefficient of $\sigma_g = d_{84}/d_{50} \leq 1.3$). Keulegan's equation (S12) underestimates flow friction for relative submergences below 10. Empirical equations such as Eqs. (S13) and (S16) capture the mean trend, but it should also be noted that point measurements of flow velocities lead to significant data scatter around the mean trend.

The occurrence of sediment transport has two important consequences regarding energy dissipation: beds usually develop bedforms, which cause additional energy dissipation (a process called form friction) due to stronger vorticity and/or surface waves, and part of the water's energy is imparted to the sediment. Sediment transport thus causes higher energy dissipation, except under certain flow conditions in which sediment deposition between bedforms smooths out bed irregularities and thereby reduces form friction (Omid et al., 2010; Hohermuth and Weitbrecht, 2018). Figure S5 shows how the friction coefficient f varies with relative submergence when sediment transport causes the formation of morphological structures along the bed in laboratory flume experiments for mountain streams. Data scatter is significant, and it is even more significant when field data are plotted.

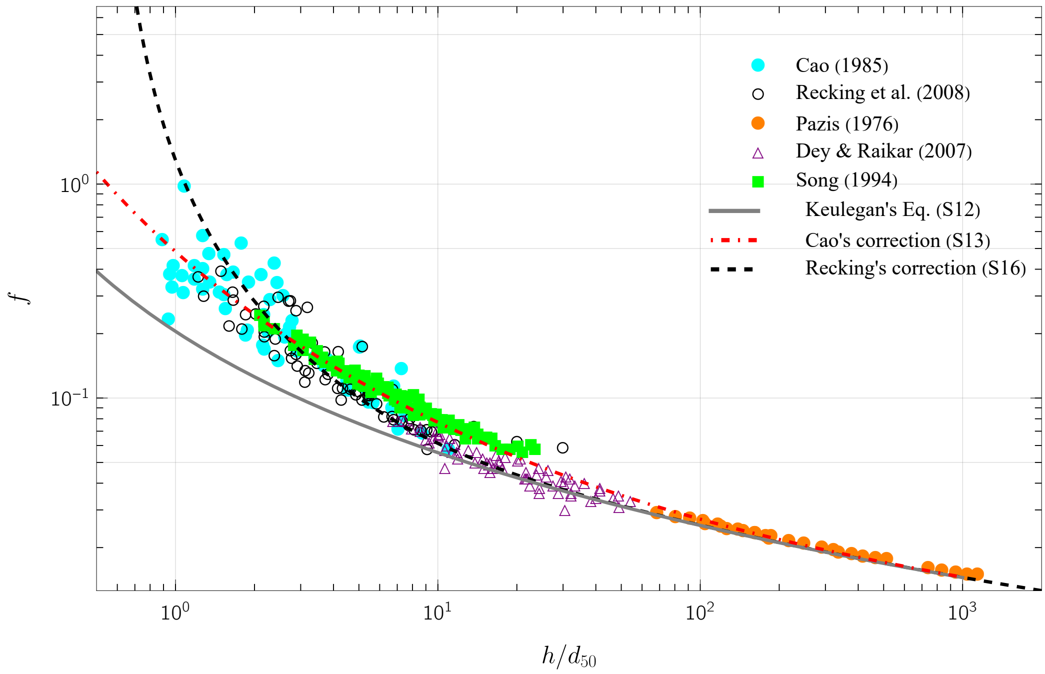

Figure S4. Variation in the friction coefficient f with relative submergence h/d_{50} for plane beds made of well-sorted gravel. Keulegan's equation (S12) is reported together with the modifications proposed by Recking et al. (2008a)—see Eq. (S16)—and Cao (1985)—see Eq. (S13). The experimental data were extracted from the theses by Pazis (1976) (d_{50} in the 0.5–3-mm range, gradation coefficient $\sigma_g = d_{84}/d_{50} = 1.1$), Cao (1985) ($d_{50}$ in the 11–44-mm range, $\sigma_g = 1.2 - 1.3$), and Song (1994) ($d_{50} = 12.3$ mm, $\sigma_g = 1.3$), and the articles by Dey and Raikar (2007) (d_{50} in the 4.1–14.2-mm range, $\sigma_g = 1.2$) and Recking et al. (2008a) (d_{50} in the 2.3–12.5-mm range, $\sigma_g = 1.1$).

Given how diversely bedforms affect the velocity field, there is no all-purpose treatment for the additional energy dissipation due to bedforms, but many bespoke methods have been developed for particular types of bedforms. The common assumption is that energy dissipations at the grain and bedform scales are additive—which means that the total friction can be broken down into skin and form frictions, respectively, and each contribution can be evaluated separately. As bedforms usually imply sediment transport, form friction also includes energy transfers from the water to the sediment. Indeed, for dunes, several methods have been proposed to estimate energy dissipation as a function of dune dimensions (Einstein, 1950; Engelund, 1966; Alam and Kennedy, 1969; van Rijn, 1984). Field surveys reveal that these methods explain part of the variance in the f variations (de Lange et al., 2021).

Sediment transport's effect on flow resistance is easier to estimate when there is no bedform or when bedforms play a negligible part in energy dissipation. These flow configurations are met when the bed remains flat, which can occur at low or high water discharges when all bedforms have been destroyed (flow conditions referred to as lower and upper regimes, respectively) or when water flows over antidunes under supercritical flow conditions (the free surface is then in phase with bed undulations). Most authors consider that the Darcy–Weisbach coefficient f, derived from Keulegan's equation (S12), remains valid insofar as the roughness size k_s is reevaluated. For sand beds, k_s is often found to depend on the median particle diameter and the Shields number (Wilson, 1989; Camenen et al., 2006). For gravel beds with a slope $i \geq 1\%$, Recking et al. (2008b) found that k_s was a multiple of the coarse grain size d_{84}:

$$k_s = \alpha_b(\xi, i) d_{84}, \tag{S17}$$

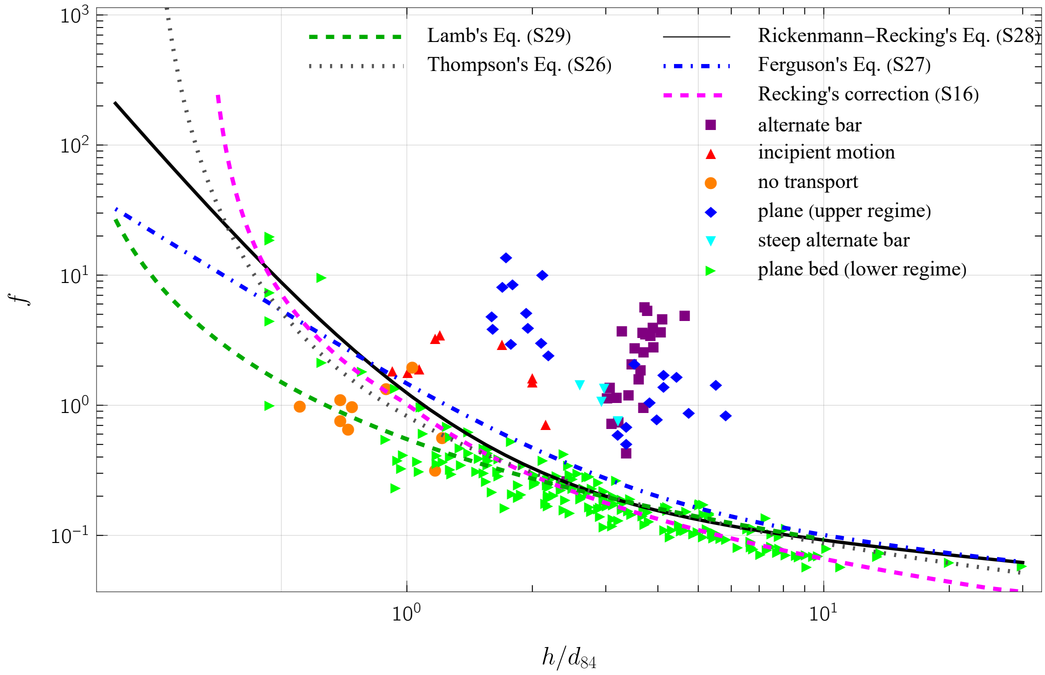

Figure S5. Variation in the friction coefficient f with relative submergence h/d_{84} for steep-flume data obtained by Cao (1985), Recking et al. (2008b), Lamb et al. (2017), and Palucis et al. (2018) for various bedforms. Recking's variant (S16) to Keulegan's equation is shown. We have also plotted empirical equations proposed by Thompson and Campbell (1979), Ferguson (2007), Rickenmann and Recking (2011), and Lamb et al. (2017) (see S2.2 for the detail). Bed slopes ranged from 0.38% to 30%. Data with sediment transport were obtained for slopes $i \geq 10$ %.

where the multiplying factor α_b is a function of the relative submergence $\xi = h/d_{84}$ and bed slope i—see Eq. (S24) in S2. A consequence of this dependence on h/d_{84} is that flow resistance is constant over a certain range of flow depths corresponding to incipient and weak sediment transport. Figure S6 compares flume data with and without sediment transport. Other authors looked more carefully at the velocity profiles (Gust and Southard, 1983; Dey and Raikar, 2007; Nikora and Goring, 2000; Gaudio et al., 2011; Dey et al., 2012; Guta et al., 2022) and found that von Kármán's constant deviated from its standard value of $\kappa = 0.41$ for clear water flows, ranging from $\kappa = 0.29$ (Nikora and Goring, 2000) to $\kappa = 0.42$ (Dey et al., 2012). In clear water flows, the mixing length ℓ_m (used in Prandtl's parametrization of wall turbulence) varies linearly with the distance y from the wall: $\ell_m = \kappa y$. When the water flow carries particles along the bed, water velocity fluctuations are damped, leading to a decrease in the mixing length. Empirical equations based on a constant value of κ and a varying roughness—such as Eq. (S17) proposed by Recking et al. (2008b)—do not contradict this behavior but merely consider that turbulence damping can be reflected by an increased roughness size.

Since we are here concerned with the estimation of flow resistance in Bagnold's equation (8), we focus on simple bed geometries (plane beds) for which flow resistance can be approximated using Keulegan's equation (S12), with $k_s = \alpha_{rl}\alpha_b d_{84}$, where the coefficient α_b is given by Eq. (S24). We will not consider the effects of bedforms on flow resistance and, thus, on bedload transport. We should, however, keep in mind that bedforms such as alternate bars can increase flow resistance by a factor of 3 to 50 (see Fig. S5) and thus reduce bedload transport rates by a factor 2 to 7 if $\Phi \propto f^{-1/2}$, as predicted by Bagnold's model (8). We also note that, broadly speaking, Bagnold's partitioning into three flow regimes is consis-

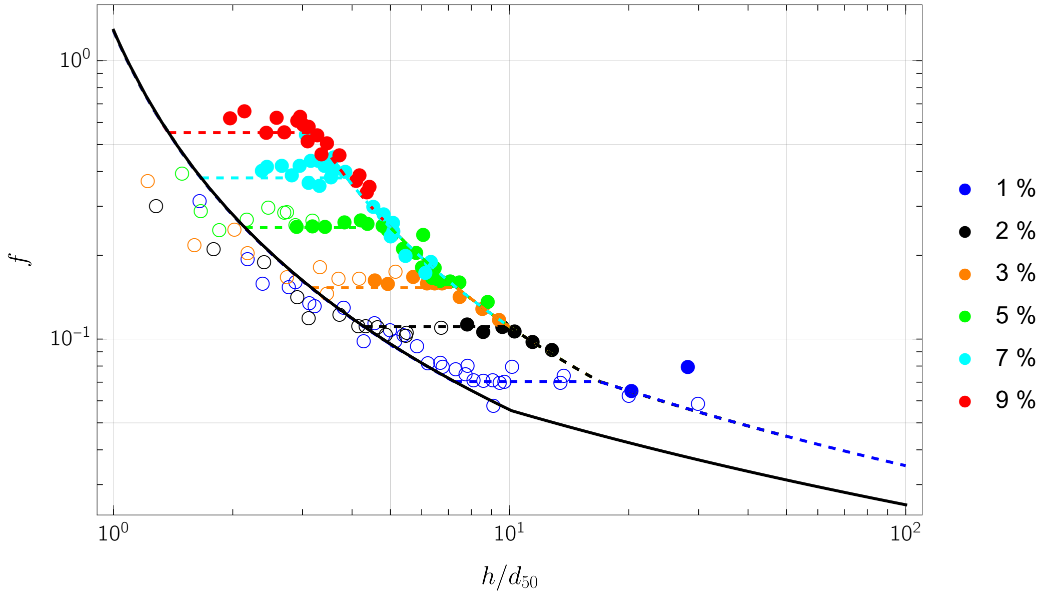

Figure S6. Variation in the friction coefficient f with relative submergence h/d_{84} for bed slopes i ranging from 1% to 9%. Keulegan's equation (S12) with $k_s = d_{84}$ is shown as a solid line. The dashed line shows Keulegan's equation (S12) when the roughness size is defined as $k_s = \alpha_{rl}\alpha_b d_{84}$. The $\circ$ symbol refers to clear water flows, whereas colored $\bullet$ symbols indicate the occurrence of sediment transport. Data from Recking et al. (2008a).

tent with Recking's observations in laboratory flumes and in the absence of bedforms. The transitional regime identified by Bagnold ($\tau_c^* \leq \tau^* \leq \tau_x^*$) and associated with low bedload transport rates is related to Recking's Domain 2 ($\xi_{12} \leq \xi \leq \xi_{23}$), which is associated with constant flow resistance (see S2). If we assume a perfect match between Bagnold's regimes and Recking's domains, then we deduce from Eq. (S21) that $\tau_c^* = i\xi_{12}/s = 0.13 i^{0.25}$, and from Eq. (S22) that $\tau_x^* = i\xi_{23}/s = 0.3 i^{0.25}$. For a slope of $i = 1\%$, these relationships predict $\tau_c^* = 0.05$ and $\tau_x^* = 0.10$, which are both realistic values.

S2 Flow Resistance

S2.1 Recking's equation

On the basis of his experiments and existing data, Recking (2006) found that flow resistance data depended on the relative submergence $\xi = h/d$, bed slope i, and the regime of sediment transport:

- No sediment transport (Domain 1) for $\xi < \xi_{12}$

$$\frac{\bar{u}}{u_*} = \sqrt{\frac{8}{f}} = \begin{cases} 6.25 + 5.75 \log \xi & \text{for } \xi > 10, \\ 2.5 + 9.5 \log \xi & \text{for } \xi \leq 10, \end{cases} \tag{S18}$$

- Weak sediment transport (Domain 2) for $\xi_{12} \leq \xi < \xi_{23}$

$$\frac{\bar{u}}{u_*} = \sqrt{\frac{8}{f_c(i)}} = \begin{cases} -3.7 - 7.18 \log i & \text{for } i \geq 0.01, \\ 1 - 4.84 \log i & \text{for } i < 0.01, \end{cases} \tag{S19}$$

According to Recking et al. (2008b), "Domain 2 is characterized by low bedload transport with a non-continuous and non-uniform bedload layer. Low-relief bed waves were observed that were no more than one grain-diameter thick and the wavelength increased when bedload increased." Recking (2006) corroborated Song's results about the constancy of the flow resistance factor in this domain (Song et al., 1994, 1998).

- Intense sediment transport (Domain 3) for $\xi > \xi_{23}$:

$$\frac{\bar{u}}{u_*} = \sqrt{\frac{8}{f}} = \begin{cases} 3.6 + 5.75 \log \xi & \text{for } \xi > 17, \\ -1.0 + 9.50 \log \xi & \text{for } \xi \leq 17. \end{cases} \tag{S20}$$

  According to Recking et al. (2008b), "Domain 3 is characterized by intense bedload transport over a flat bed with a uniform bedload layer that was several grain-diameters thick."

Recking et al. (2008b) defined that the limits ξ_{12} between Domains 1 and 2 can be expressed as a power function of bed slope i:

$$\xi_{12} = \begin{cases} 0.223 i^{-0.756} & \text{for } i \geq 0.01, \\ 0.695 i^{-0.509} & \text{for } 0.007 \leq i < 0.01, \\ 0.135 i^{-0.841} & \text{for } i < 0.007, \end{cases} \tag{S21}$$

while the limit ξ_{23} between Domains 2 and 3 can be written

$$\xi_{23} = \begin{cases} 0.52 i^{-0.756} & \text{for } i \geq 0.01, \\ 0.35 i^{-0.841} & \text{for } i < 0.01. \end{cases} \tag{S22}$$

It is possible to generate a formulation that combines all the equations above into a single expression. To that end, let us define the coefficients

$$\alpha_1(\xi) = 4.5 \frac{(1 + (\xi/10)^2)^{0.325}}{\xi^{0.65}} \text{ and } \alpha_3(\xi) = 18.2 \frac{(1 + (\xi/17)^2)^{0.325}}{\xi^{0.65}}, \tag{S23}$$

that can may be used to define two Keulegan-like curves:

- the first curve corresponds to the no transport domain (Domain 1): $\bar{u}/u_* = 6.25 + 5.75 \log(\xi/\alpha_1)$;
- the second curve is related to intense sediment transport (Domain 3): $\bar{u}/u_* = 6.25 + 5.75 \log(\xi/\alpha_3)$.

The coefficients α_1 and α_3 describe the potential increase in the bed roughness owing to low submergence conditions (Domain 1) and bedload transport (Domain 3). To generate a single roughness function, we define the generalized roughness coefficient:

$$\alpha_b(\xi,i) = \begin{cases} \alpha_1 & \text{for } \xi < \xi_{12} \\ \alpha_3 \xi/\xi_{23} & \text{for } \xi_{12} \leq \xi < \xi_{23} \\ \alpha_3 & \text{for } \xi > \xi_{23}. \end{cases} \tag{S24}$$

The generalized Keulegan equation is then

$$\frac{\bar{u}}{u_*} = \sqrt{\frac{8}{f}} = 6.25 + 5.75 \log \frac{\xi}{\alpha_b(\xi,i)}. \tag{S25}$$

Figure S7 shows several side-view images of a shallow supercritical flow over a gravel bed alongside a graph of the Darcy–Weisbach coefficient f taken from the experiments run by Recking (2006). The friction coefficient f responds differently to an increase in the bottom shear stress. For $\xi < \xi_{23}$, the Darcy–Weisbach coefficient f is close to the constant value $f_c(0.05) = 0.25$, whereas for $\xi > \xi_{23}$, it starts to decrease by following the trend given by Eq. (S20). The side-view images indicate that for Domain 2 (weak sediment transport), represented by points 1 and 2 in the graph, the bedload layer is thin (its thickness is of the order of d_{84}); however, for Domain 3 (intense sediment transport), illustrated by points 3 and 4, the bedload layer is thicker.

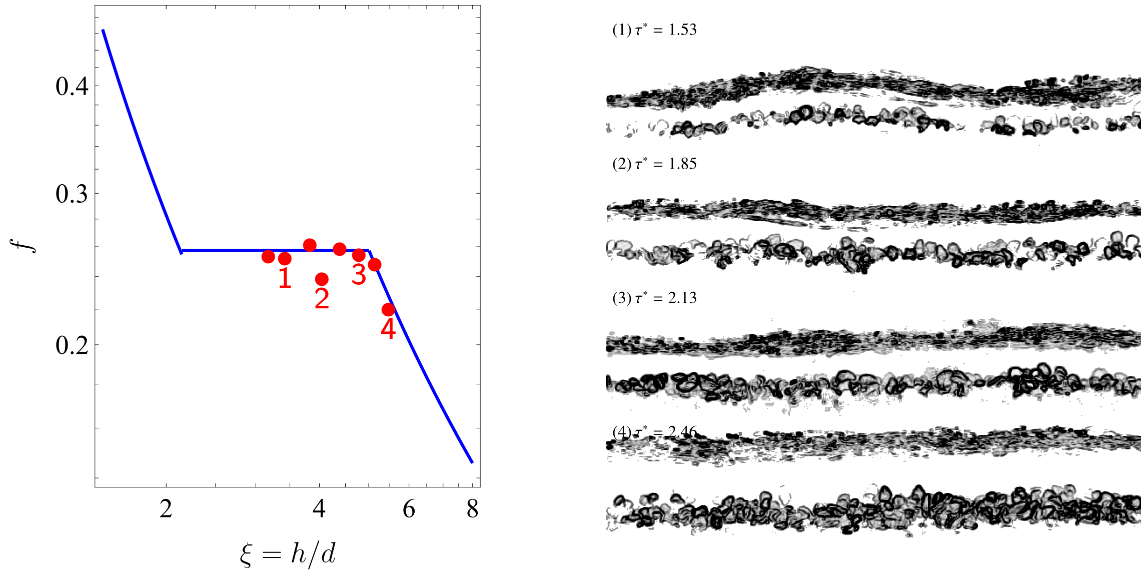

Figure S7. Variation in the friction coefficient f measured by Recking (2006) and predicted using Recking's equation (S25). We also show side-view images of the flume experiment conducted by Recking (2006) using a slope of $i = 5\%$ and a gravel bed with a median size of $d_{50} = 4.9$ mm. By subtracting two images, the author determined what had moved and what had stayed in the same place. Moving grains and the free surface appear in white, while the rest is black. The full sequence of f values related to this slope is shown in Fig. S6.

S2.2 Other empirical equations

Thompson and Campbell (1979) considered that flow resistance increases in shallow flows because of (i) the additional drag on flow exerted by large bed protuberances and (ii) stress concentration over the finer bed elements generated by obstructing protuberances. They added a correcting factor of $0.1k_s/h$ to Keulegan's equation:

$$f = \left(2.3\left(1 - 0.1\frac{k_s}{h}\right)\log\left(\frac{12.2h}{k_s}\right)\right)^{-2}, \tag{S26}$$

with $k_s = 4{,}5d_{50}$ or $k_s = 2.37d_{84}$. For mountain streams exhibiting shallow flows, Ferguson (2007, 2021b) proposed the following equation, which he called the variable-power equation:

$$\sqrt{\frac{8}{f}} = \frac{a_1 a_2 \dfrac{h}{k_s}}{\left(a_1^2 + a_2^2\left(\dfrac{h}{k_s}\right)^{5/3}\right)^{1/2}}, \tag{S27}$$

with $a_1 = 6.5$ et $a_2 = 2.5$ and $k_s = d_{84}$. This equation is consistent with the Manning–Strickler equation for $h/k_s > 10$. Rickenmann and Recking (2011) compiled 27 studies (with a total of 2,890 measurements) related to water discharge and velocity in gravel-bed rivers whose slopes ranged from $4 \times 10^{-3}\%$ to 24%. They proposed the following empirical equation for f:

$$\sqrt{\frac{8}{f}} = 4.416\left(\frac{h}{d_{84}}\right)^{1.904}\left(1 + \left(\frac{h}{1.283d_{84}}\right)^{1.618}\right)^{-1.083}. \tag{S28}$$

Lamb et al. (2017) considered that Prandtl's mixing length is modified when the flow is shallow, resulting in this equation for f:

$$f = 8\left(\kappa^{-1}\log\left(1+\frac{30h}{k_s}\right) - \kappa^{-1}\right)^{-2}, \tag{S29}$$

with $k_s = 2.5d_{84}$.

S3 Microstructural studies of bedload transport

Here are additional remarks about some of the theoretical and numerical results reported in Table 6 in the review article.

Armanini et al. (2005) investigated intense bedload transport flows on a conveyor belt. They observed different regimes depending on bed slope and Froude number: sheet flows (immature debris flows), mature flows (debris flows), and bed failure (loose bed). They showed that the bedload transport rate scaled as a linear function of the water discharge:

$$q_s = c_s q \tag{S30}$$

where c_s is the bedload concentration, which is a function of bed slope:

$$F = \begin{cases} \dfrac{\varrho}{\Delta\varrho}\dfrac{\tan\theta}{\tan\phi - \tan\theta} & \text{for } \theta \leq \theta_c, \\ \dfrac{\varrho}{\Delta\varrho}\dfrac{\tan\theta_c}{\tan\phi - \tan\theta_c} & \text{for } \theta > \theta_c, \end{cases} \tag{S31}$$

where $\phi = 31^\circ$ and $\theta_c = 8^\circ$ in their experiments. They also observed that the material behaved like a frictional material when the Bagnold number defined as

$$\mathrm{Ba} = \frac{\varrho_s}{\eta}\sqrt{\lambda}d^2\dot{\gamma}, \text{ with } \lambda = \frac{1}{(c_{max}/c_s)^{1/3} - 1} \tag{S32}$$

(where $c_{max} = 0.74$ is the maximum concentration) was lower than 10^3, and the material behaved like a collisional (Bagnold) fluid for $\mathrm{Ba} > 10^3$. They observed a layered structure in which particles experienced frictional contacts ($\mathrm{Ba} < 10^3$) near the bottom but were in a collisional regime in the upper layer. Although the frictional and collisional regimes described local behaviors, we can try to define a bulk transition. In terms of Shields numbers, the transition from the viscous regime to the collisional regime occurred at approximately

$$\tau^*_{vc} = 10^3\frac{\varrho}{\varrho_s}\lambda^{-1/2}R^{-2} \sim \frac{200}{R^2}. \tag{S33}$$

If we consider that flow resistance could be estimated using the Darcy–Weisbach equation, then it is possible to recast equation (S30) in a dimensionless form:

$$\Phi = \frac{F(\theta)}{\sin\theta}\sqrt{\frac{8}{f}}s^{3/2}\tau^{*3/2}. \tag{S34}$$

The sheet-flow regime is expected to be substantially influenced by particle collisions.

Some authors have rescaled the Shields number and the transport rate.

- Capart and Fraccarollo (2011) obtained $\tilde{\Phi} = 4\cos\theta\Phi^{3/2}$ by redefining the Shields number: $\tilde{\tau}^* = h\tan\phi\tan\theta/(ds(\tan\phi - \tan\theta))$.

- Pähtz and Durán (2020) rescaled the dimensionless Shields number and the transport rate to account for the influence of bed slope:

$$(\tilde{\tau}^*, \tilde{\Phi}^2) = (\tau^*, \Phi^2)\Big/\left(\cos\theta - \frac{\sin\theta}{\mu_b}\frac{1}{s}\right), \tag{S35}$$

where μ_b denotes the Coulomb particle-bed friction coefficient. They did not change the critical Shields number, however, and this resulted in:

$$\tilde{\Phi} \approx \sqrt{\tau_c^*}(\tilde{\tau}^* - \tau_c^*)(1 + c_m(\tilde{\tau}^* - \tau_c^*)/\mu_b). \tag{S36}$$

- For the same reason, but pursuing a different line of thinking, Maurin et al. (2018) redefined the Shields number as:

$$\hat{\tau}^* = \tau^*/(\mu_s(1 - \tan\theta/\tan\theta_0)) \ , \tag{S37}$$

where μ_s is the granular friction coefficient and θ_0 is the critical angle for the onset of bed failure defined by Takahashi (1981):

$$\tan\theta_0 = \frac{\mu_s}{1 + (sc_{max})^{-1}}, \tag{S38}$$

where c_{max} is the maximum packing fraction.

S4 Additional figures

S4.1 Scaling stream power differently

Revisiting Bagnold's latest articles, Parker et al. (2011) and Ferguson (2012) suggested scaling stream power with particle diameter d_{50}

$$\omega^* = \frac{\omega}{\varrho(sgd_{50})^{3/2}}. \tag{S39}$$

Although these authors focused on critical stream power ω_c^*, we can extend their analysis and propose the scaling law

$$\Phi = m(\omega^* - \omega_c^*) \tag{S40}$$

with $m \sim 1$. Figure 8 shows how this equation compares with laboratory and field data. Following Ferguson (2021a), we grouped the data depending on particle diameter d_{50}. This scaling captures the overall trend.

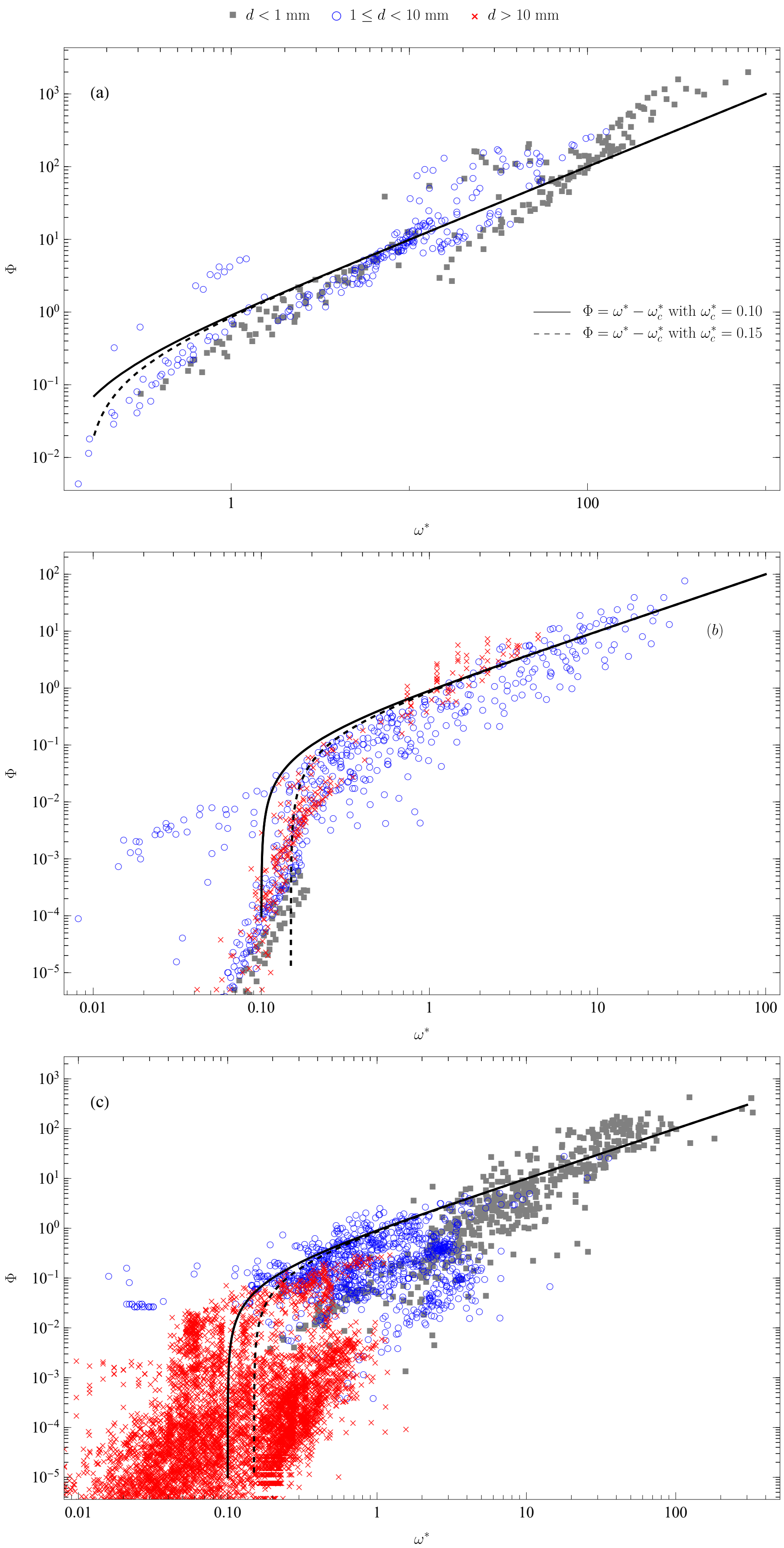

Figure S8. Variation in Φ with ω^*. The solid and dashed lines show Eq. (S40) with $\omega_c^* = 0.10$ and $\omega_c^* = 0.15$, respectively, and $m = 1$. (a) Pipe-flow data used in Fig. 2. (b) Flume data used in Figs. 3–4. (c) Field data used in Fig. 5.

S4.2 Scaling the Shields stress differently

In Figs. 2 to 5 in the review paper's body, we used the median diameter d_{50} in the definition of the dimensionless shear stress τ^* and bedload transport rate Φ:

$$\tau^* = \frac{\tau_b}{(\varrho_s - \varrho)gd_{50}}, \text{ and } \Phi = \frac{q_s}{\sqrt{sgd_{50}^3}} \tag{S41}$$

where $\tau_b = \varrho g R_h i$ denotes the bottom shear stress (for steady uniform flows), and q_s is the bedload transport rate per unit width. To recall that these quantities were defined based on the median grain size, we will refer to them as τ_{50}^* and Φ_{50}. We could have preferred to use the coarse grain diameter d_{84} in these definitions

$$\tau_{84}^* = \frac{\tau_b}{(\varrho_s - \varrho)gd_{84}} \text{ and } \Phi_{84} = \frac{q_s}{\sqrt{sgd_{84}^3}}. \tag{S42}$$

Figure S9 shows how scaled bedload transport rates vary with dimensionless shear stresses depending on the characteristic diameter chosen. We have also plotted Bagnold's master curve

$$\Phi = (10\tau^*)^{16}\left(1+\left(\frac{\tau^*}{\tau_1^*}\right)^{3/2}\right)^{-8/9}\left(1+\left(\frac{\tau^*}{\tau_0^*}\right)^{8}\right)^{-13/8}, \tag{S43}$$

with $\tau_0^* = 0.078$ and $\tau_1^* = 0.40$. We did not use all the data, but those presented in § S5.3 (5272 data in all), which cover a wide range of Shields stress (three orders of magnitude from $\tau^* = 0.01$ to $\tau^* = 10$) and come from various rivers across the world. Overall, there is not much difference between the two plots, but taking a look at the details, we can detect some slight differences. In particular, scaling Shields stresses and transport rates with d_{84} produces less noisy data for $\tau^* > 0.10$. It comes as no surprise that there is a better match between Bagnold's master curve and data based on the median diameter since the former has been adjusted using quantities scaled with the median diameter. We have to recalibrate Bagnold's master equation when working with the coarse grain diameter d_{84}.

The easiest way to rescale Bagnold's master curve is to assume a constant d_{84}/d_{50} ratio: for the data presented in § S5.3, we obtain $d_{84}/d_{50} = 3.6$, and the readjusted Bagnold's master equation is

$$\Phi_{84} = \left(\frac{d_{50}}{d_{84}}\right)^{3/2}\Phi_{50} = (32\tau_{84}^*)^{16}\left(1+\left(\frac{\tau_{84}^*}{\tau_{84,1}^*}\right)^{3/2}\right)^{-8/9}\left(1+\left(\frac{\tau_{84}^*}{\tau_{84,0}^*}\right)^{8}\right)^{-13/8}. \tag{S44}$$

with $\tau_{84,0}^* = 0.0215$ and $\tau_{84,1}^* = 0.111$.

A number of works have suggested that bedload transport rates scale with the deviation $\tau^* - \tau_c^*$ from the threshold of incipient motion τ_c^* rather than τ^* alone. Taking this suggestion into account presents two issues here. First, there is no consensus about the value of the threshold of incipient motion τ_c^*, in particular for bed with a wide grain size distribution on steep slope. Second, using the difference $\tau^* - \tau_c^*$ in a log-log plot leads to remove all data for which $\tau^* < \tau_c^*$. We settled these issues as follows.

As an approximation to the threshold of incipient motion τ_c^*, we use the equation proposed by Recking (2009), which includes a dependence on bed slope i and sediment gradation $\sigma_g = d_{84}/d_{50}$

$$\tau_c^* = (1.32i + 0.037)\sigma_g^{-0.93}. \tag{S45}$$

To settle the second issue, we plot bedload transport rates as a function of τ^*/τ_c^* instead of $\tau^* - \tau_c^*$. Figure S10 shows how scaled bedload transport rates vary with the shear stresses ratio τ^*/τ_c^* depending on the characteristic diameter chosen. The effect of this change of

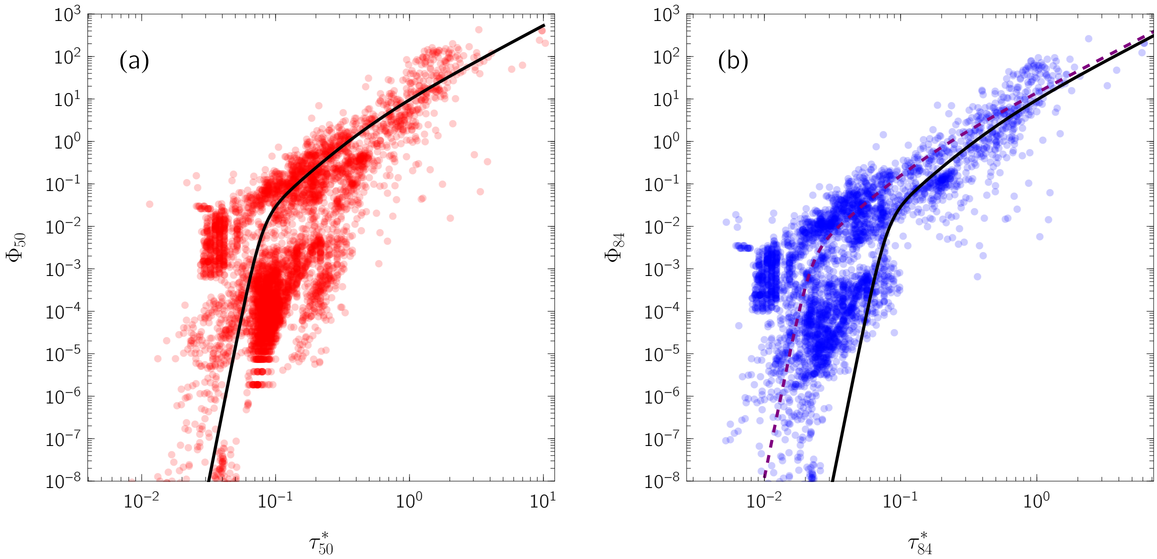

Figure S9. (a) Variation in Φ with τ^* with the median diameter d_{50} as the characteristic diameter. (b) Variation in Φ with M. (b) Variation in e_b with τ^*. The solid line shows Bagnold's master equation (S43) based on the median diameter. The dashed line shows Bagnold's master equation (S44) recalibrated to be based on the coarse grain diameter d_{84}.

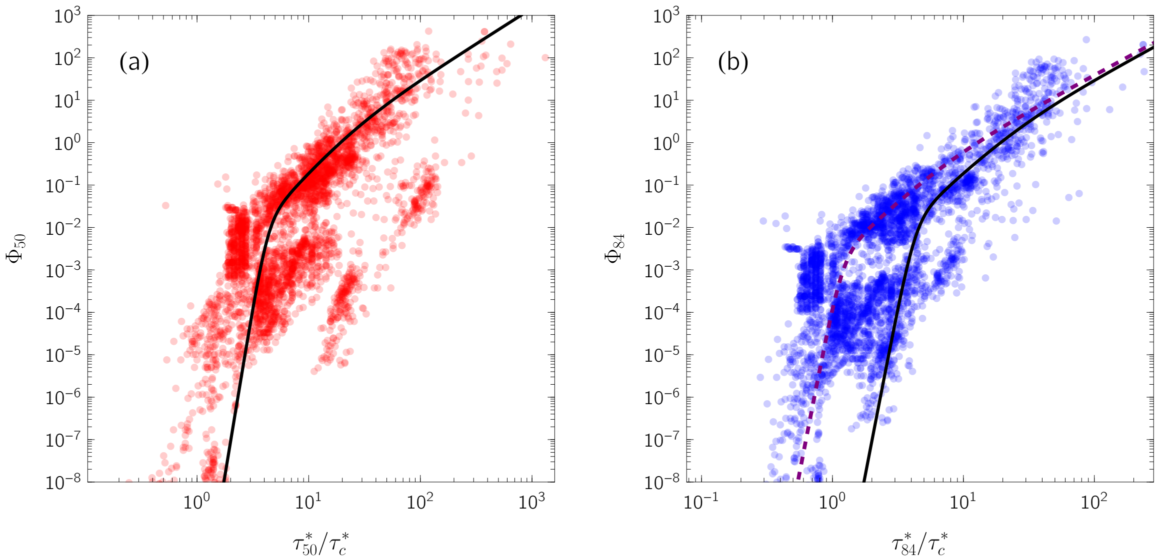

Figure S10. (a) Variation in Φ_{50} with τ^*_{50}/τ^*_c with the median diameter d_{50} as the characteristic diameter. (b) Variation in Φ_{84} with τ^*_{84}/τ^*_c. The solid line shows Bagnold's master equation (S43). For plotting this curve, we needed to define the scaled variables τ^*_{50}/τ^*_c; we evaluated τ^*_c was evaluated as the mean value over all the τ^*_c sample, where each element was computed from field data using Eq. (S45). We found $\bar{\tau}^*_c = 0.018$. The dashed line shows Bagnold's master equation (S44) adjusted for the coarse diameter d_{84}.

variable is to slightly reduce the data scatter at low Shields stresses (for the rarefied transport regime).

Measuring the hydraulic radius in shallow flows over coarse beds is fraught with uncertainties, and using the resulting value to estimate bed shear stresses may also be problematic (Yager et al., 2019). One can wonder whether we can overcome this difficulty by considering effective cross-sections. Redolfi et al. (2016) have showed that from place to place along a reach, cross-section can vary, but it remains statistically equivalent to an effective power-law profile. Here, we assume that when knowing water discharges, we can estimate effective flow depths. To that end, we assume that flow velocity $\bar{u}$ and water discharge q (per unit width) are related to each other by the following empirical equation proposed by Rickenmann and Recking (2011), who refined the variable-power equation developed by Ferguson (2007):

$$\bar{u}^* = 1.5471 q^{*0.7062} \left(1 + \left(\frac{q_*}{10.31}\right)^{0.6317}\right)^{-0.493}, \tag{S46}$$

with

$$\bar{u}^* = \frac{\bar{u}}{\sqrt{gid_{84}}} \text{ and } \bar{q}^* = \frac{q}{\sqrt{gid_{84}^3}} \tag{S47}$$

from which we deduce an effective flow depth h_e:

$$\frac{h_e}{d_{84}} = \frac{q^*}{\bar{u}^*} = 0.65 q^{*-0.3} \left(1 + \left(\frac{q_*}{10}\right)^{0.63}\right)^{0.49}. \tag{S48}$$

As shown by Fig. S11, comparing hydraulic radius R_h and effective flow depth h_e reveals that for $R_h < 200 d_{84}$, Eq. (S48) predicts hydraulics radius to within 30%. For deeper flows, the precision is lower. We computed an effective Shields stress $\tilde{\tau}_*$ based on this effective flow depth h_e

$$\tilde{\tau}_* = \frac{ih_e}{sd_x},$$

with $d_x = d_{50}$ or $d_x = d_{84}$. Figure S12 shows how scaled bedload transport rates Φ vary with the effective shear stresses ratio $\tilde{\tau}^*/\tau_c^*$ depending on the characteristic diameter chosen. The effect of this change of variable is to reduce the data scatter around the mean trend apart from a data subset that deviates significantly from this mean trend. When using the coarse diameter d_{84}, this subset is closer to the rest of data, but Bagnold's master curve (S43)—based on the median diameter—underestimates bedload transport rates.

This comparison shows that for shallow flows on coarse gravel beds, using Rickenmann–Recking's equation (S48) can be used to evaluate the Shields stress. Using the coarse diameter d_{84} may also lead to slight less noisy estimates of bedload transport, but this choice implies that Bagnold's master equation be adjusted using the coarse diameter rather than median diameter.

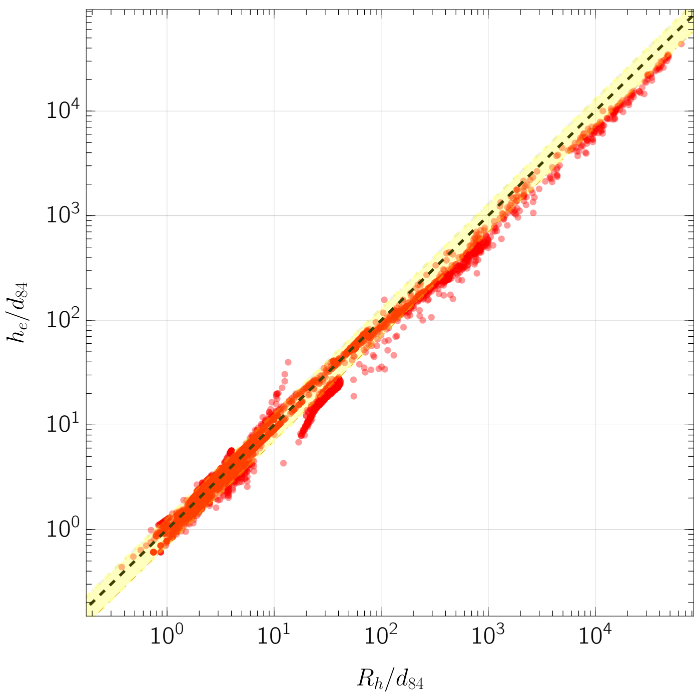

Figure S11. Comparison between the measured hydraulic radius and estimated flow depth h_e. The yellow band around the line of perfect equality shows the $\pm 30\%$ variation around $h_e = R_h$.

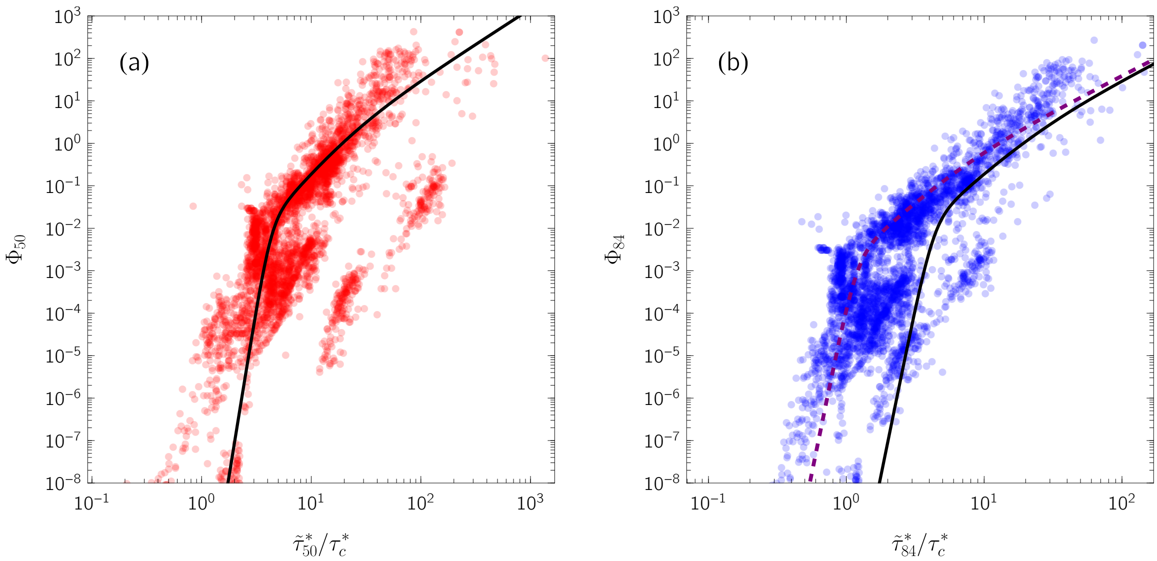

Figure S12. (a) Variation in Φ_{50} with τ^*_{50}/τ^*_c with the median diameter d_{50} as the characteristic diameter. (b) Variation in Φ_{84} with τ^*_{84}/τ^*_c. The solid line shows Bagnold's master equation (S43). For plotting this curve, we needed to define the scaled variables τ^*_{50}/τ^*_c; we evaluated τ^*_c was evaluated as the mean value over all the τ^*_c sample, where each element was computed from field data using Eq. (S45). We found $\bar{\tau}^*_c = 0.018$. The dashed line shows Bagnold's master equation (S44) adjusted for the coarse diameter d_{84}.

S4.3 Parker's scaling

Working on poorly-sorted gravel bed, Parker et al. (1982) noted that scaling both bedload transport rates and Shields stress is problematic because the particle diameter d_i related to the size fraction f_i is involved in both scalings ($\Phi = q_s/\sqrt{sgd^3}$ and $\tau^* = \tau/(s\varrho g d)$). Moreover, one should differentiate between the subsurface and pavement particle diameters (bedload particles have sizes that are close to that in the subsurface layers) given the significant difference (a factor of 2 to 3) between surface and subsurface d_{50} values. Parker et al. (1982) suggested scaling transport rates and bottom stresses differently to avoid the dependence of the scaled transport rate on d:

$$W^* = \frac{\Phi}{\tau^{*3/2}} = \frac{s}{\sqrt{g}(id)^{3/2}} q_s \text{ and } \varphi = \frac{\tau^*}{\tau_r^*}. \tag{S49}$$

As we focus on the mean behavior of bedload transport, we have not partitioned the grain size distribution into different fractions f_i in these definitions as Parker et al. (1982) did. In Eq. (S49), τ_r^* is a reference Shields value. It is estimated by evaluating the bottom Shields stress for which the scaled transport rate W^* reaches the reference value $W_r^* = 0.002$. In practice, to evaluate τ_r^* from field data, we fitted a power-law function $W_* = a\tau^{*b}$ to the data, and set $\tau_r^* = (W_r^*/a)^{1/b}$.

Parker et al. (1982) also proposed the following empirical bedload transport equation:

$$W^* = \begin{cases} 0.0025 \exp\left(14.2(\varphi - 1) - 9.28(\varphi - 1)^2\right) & \text{for } 0.95 < \varphi < 1.65, \\ 11.2\left(1 - \dfrac{0.822}{\varphi}\right)^{9/2} & \text{for } \varphi > 1.65. \end{cases} \tag{S50}$$

To test this equation, we did not use all the data, but those presented in § S5.3. In this dataset, we failed to determine the reference Shields stress for 22 rivers, and in the end, we only kept data from the East Fork River, Goodwin Creek, Jacoby Creek, Jarbidge River, Oak Creek, Nahal Eshtemoa, Caspar Creek, Riedbach, and Navisence. Figure 13 shows the data scaled using Eq. (S49) (2923 data in all), Parker's equation Eq. (S50), and Bagnold's master equation. To that end, we had to define a mean reference Shields stress $\bar{\tau}_r^*$ by averaging all the reference values obtained for the rivers tested, Bagnold's master equation in the (φ, W^*) coordinate system:

$$W^*(\varphi) = 10^{16}\left(\varphi\frac{\bar{\tau}_r^*}{\tau_0^*}\right)^{29/2}\left(1 + \left(\varphi\frac{\bar{\tau}_r^*}{\tau_0^*}\right)^8\right)^{-13/8}\left((1 + \left(\varphi\frac{\bar{\tau}_r^*}{\tau_1^*}\right)^{3/2}\right)^{-8/9} \tag{S51}$$

with $\bar{\tau}_r^* = 0.054$, $\tau_0^* = 0.078$, and $\tau_1^* = 0.4$. As shown by Fig. 13, there is not much between Parker's equation Eq. (S50) and Bagnold's master equation. The data scatter is significant (two orders of magnitude), but as we did not follow Parker et al.'s procedure (by partitioning bedload transport rates by size fraction), it is impossible to draw sound conclusions about how this equation compares with Bagnold's model when applied to field data.

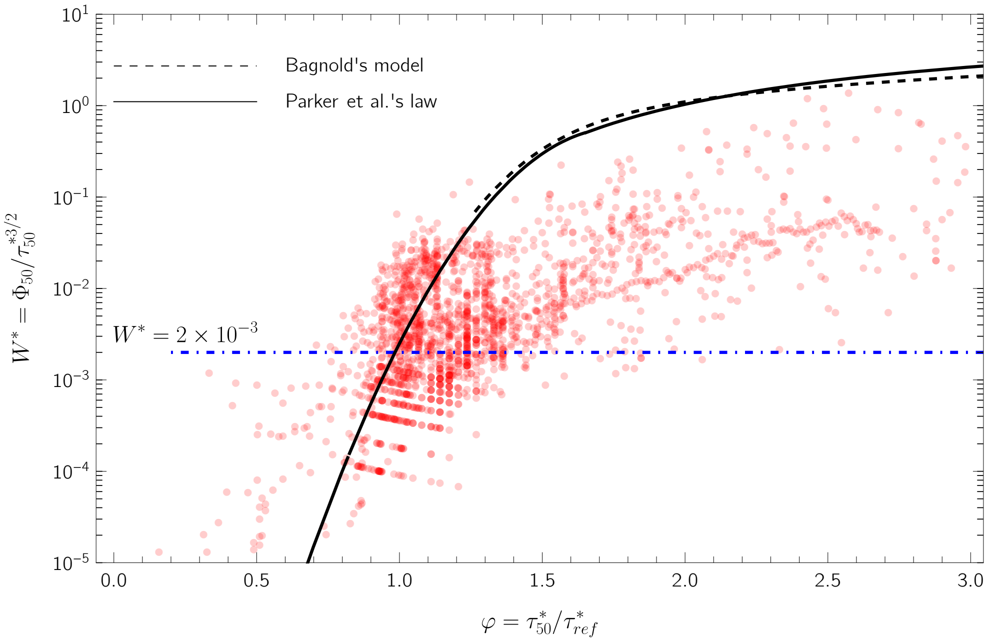

Figure S13. Variation in W^* with $\varphi*$. We have also plotted Parker's equation Eq. (S50), and Bagnold's master equation (S51). The dot-and-dash line shows the reference level $W^* = 0.002$ suggested by Parker et al. (1982) for defining the reference Shield stress τ_r^*.

S4.4 Comparison of bedload transport equations at low Shield stresses

Figure 3(a) in the review paper's body shows how bedload transport rates vary with Shield stress for laboratory flume. Here, Fig. S14 provide a close-up view of this figure for $\tau^* < 0.2$. In addition to the equations used in the article

- Bagnold's master equation (with $\tau_0^* = 0.078$ and $\tau_1^* = 0.40$)

$$\Phi = (10\tau^*)^{16} \left(1 + \left(\frac{\tau^*}{\tau_1^*}\right)^{3/2}\right)^{-8/9} \left(1 + \left(\frac{\tau^*}{\tau_0^*}\right)^{8}\right)^{-13/8}, \tag{S52}$$

- Einstein's model (with $a_1 = 0.156$, $a_2 = 2.0$, and $\alpha = 1/27$)

$$\Phi = \frac{\alpha p}{1-p} \text{ with } p = 1 - \frac{1}{\sqrt{\pi}} \int_{-a_1/\tau^* - a_2}^{a_1/\tau^* - a_2} e^{-x^2}\mathrm{d}x, \tag{S53}$$

- Einstein's approximation

$$\Phi = \frac{1}{0.465} \exp\left(\frac{-0.391}{\tau^*}\right). \tag{S54}$$

- Wang's equation (with $a_1 = 0.07$ and $a_2 = 2.0$)

$$\Phi = \frac{\alpha p}{1-p} \frac{\tau^{*3/2}}{20} \text{ with } p = 1 - \frac{1}{\sqrt{\pi}} \int_{-a_1/\tau^* - a_2}^{\infty} e^{-x^2}\mathrm{d}x, \tag{S55}$$

- Guo's equation

$$\Phi = 10\tau_*^{5/3} \exp\left(-\frac{16}{1 + (30\tau_*)^3}\right). \tag{S56}$$

- Engelund and Hansen's model (flow resistance modeled using Jäggi's parametrisation)

$$\Phi = 2.1 \left(\frac{s}{i}\right)^{1/3} \sqrt{\tau^{*2} + 0.15}\tau^{*7/3}. \tag{S57}$$

we have also plotted the empirical equation proposed by (Parker, 1978):

$$\Phi = 11.2 \frac{(\tau^* - 0.03)^{9/2}}{\tau^{*3}} \tag{S58}$$

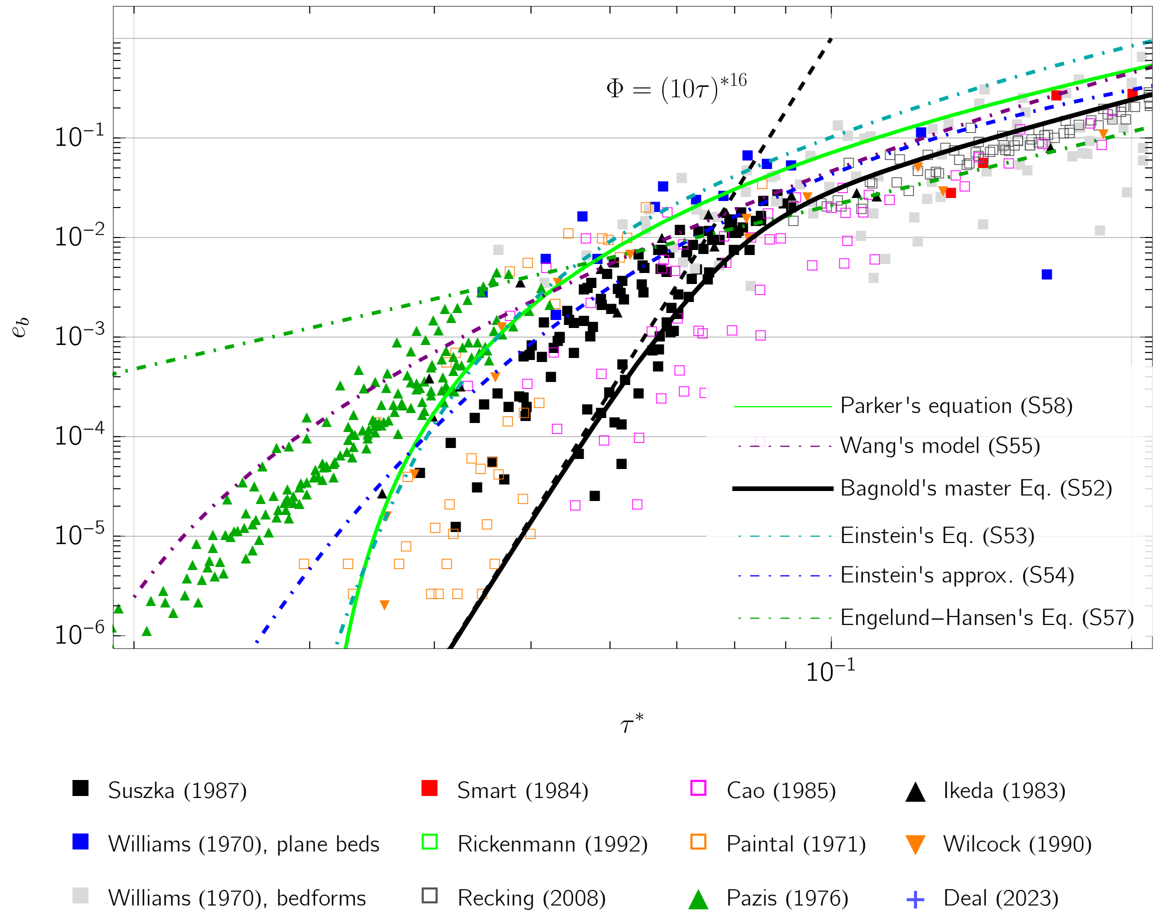

Figure S14. Close-up view of Fig. 3(a) showing the variation in the dimensionless bedload transport rate Φ with the dimensionless shear stress (for $\Phi \leq 1$) and comparison with the revised Bagnold model (42), Einstein's model (44) and Einstein's empirical equation (44), Wang's equation (45), and Engelund–Hansen's equation (48) (evaluated with $i = 1\%$ and $s = 1.65$). Equation numbers refer to equations in the review article.

S4.5 Selection of sites

In our application to Bagnold's master equation to real-world rivers, we found that for 17 rivers, there is a good match between Bagnold's master equation (S44) and field data. Figure S15(a) and (b) show how bedload transport rates vary with Shields stress τ_* and Martin's number M for these rivers, and Fig. S15(c) shows the variation in the efficiency factor with Shield stress.

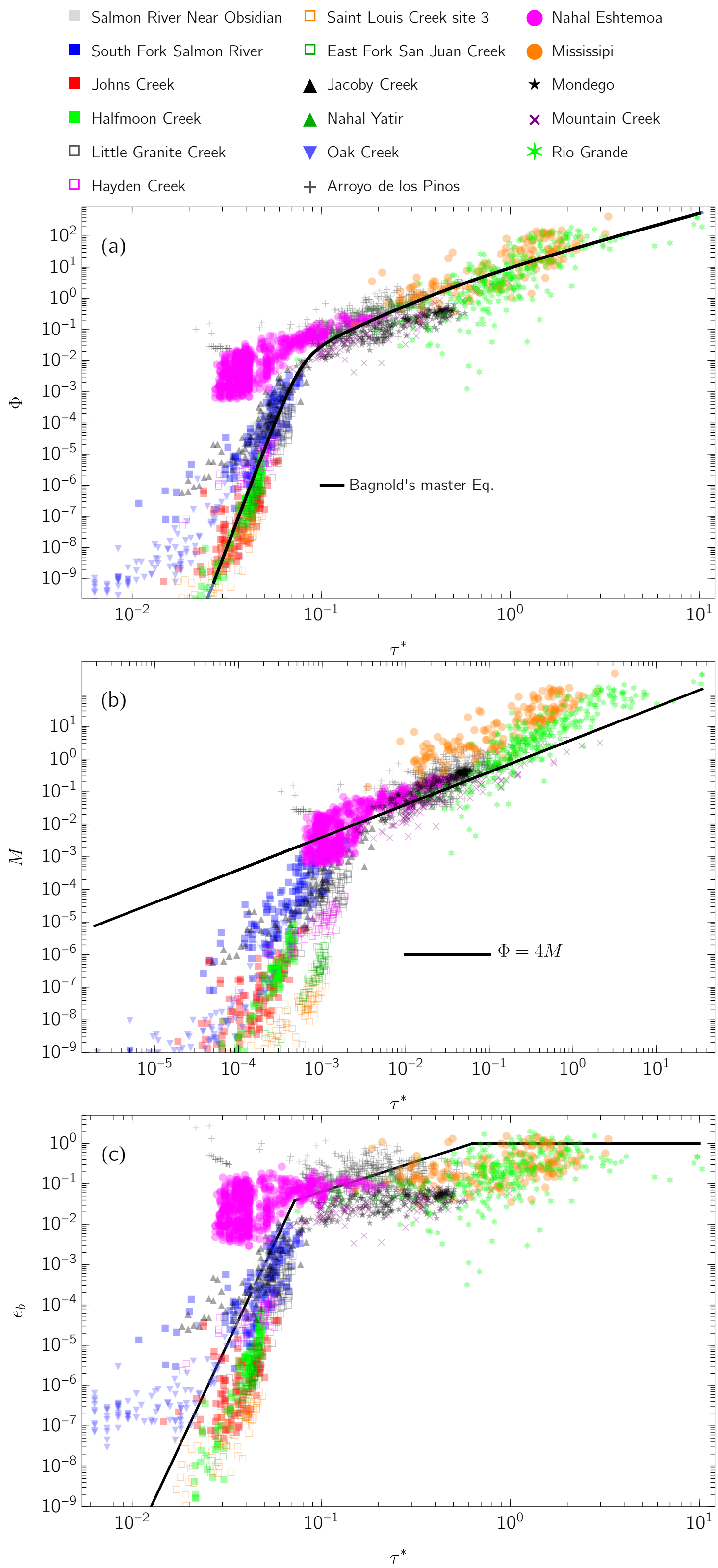

Figure S15. (a) Variation in Φ with τ^* for gravel-bed rivers depending on the main type of bedforms at the monitoring station. (b) Variation in Φ with M. (b) Variation in e_b with τ^*; the solid lines show the empirical trends determined in § 2.7 in the review article: $e_b = (10\tau^*)^{10}$ (rarefied transport regime for $\tau^* \leq \tau_0^*$), $e_b = 2\tau^{*1/5}$ (kinetic regime for $\tau_0^* \leq \tau^* \leq \tau_1^*$), and $e_b = 1$ (sheet flow regime for $\tau^* > \tau_1^*$).

S4.6 Effect of bedform on efficiency factor

Figure S16 shows how the efficiency factor e_b with Shields stress τ^* for different types of bedforms.

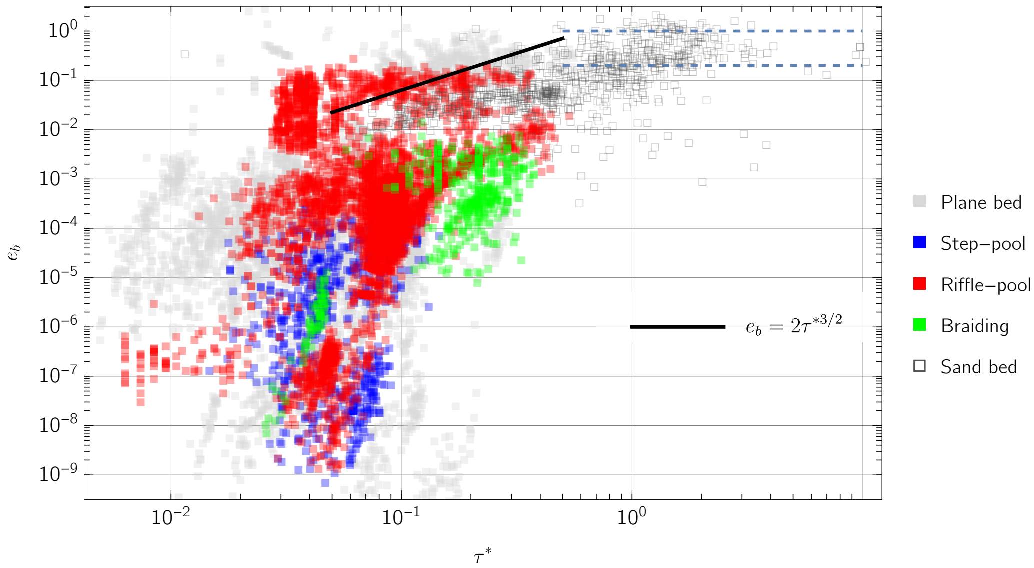

Figure S16. (a) Variation in the efficiency e_b with τ^* for different types of bedforms.

S4.7 Values of n

Figure S17 shows the value of the scaling n when fitting the power law $\Phi \propto \tau_*^n$ to the numerical data produced by models presented in Table 6 in the review article.

If there were a good match between microstructural models and Bagnold's scalings, we would have expected to obtain n close to 3 in the frictional regime (models provide n values in the 1.5–2.5 range) and close to 5/3 in the frictional-collisional regime (models provide n values in the 1.5–2.5 range). For the latter regime, some models provide n values that come close to 5/3 (Hsu et al., 2004; Berzi and Fraccarollo, 2013; Revil-Baudard and Chauchat, 2013; Maurin et al., 2018).

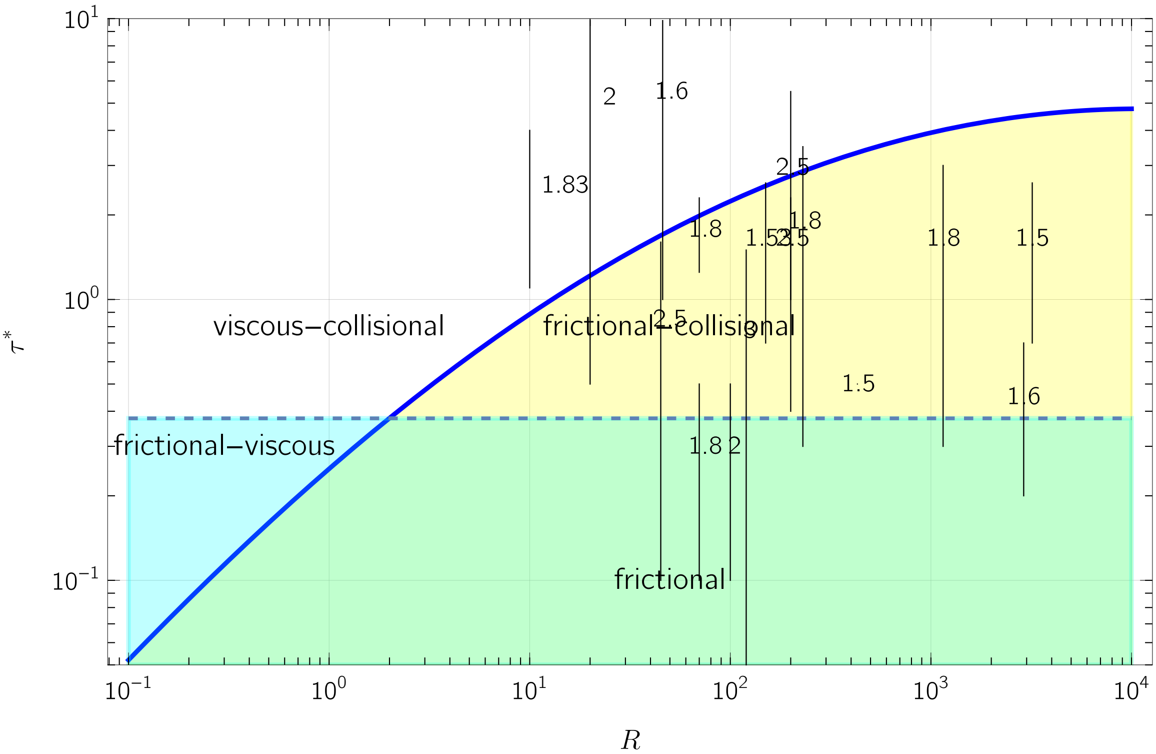

Figure S17. Contact type in the (R,τ^*) diagram (same plot as Fig. 13 in the review article). The solid line shows the transition from the frictional to the lubricated contact regimes predicted by Eq. (55) in the review paper. The dashed line shows the transition from the frictional to the collisional contact regimes predicted by Eq. (58) in the review paper. The vertical lines show the τ^* range explored by the models presented in Table 6.

S5 Sources of Data

S5.1 Sediment Transport in Idaho and Nevada

We used the database proposed by the Boise Adjudication Team (King, 2004; Whiting et al., 1999). For each stream, we used the cross-section data to derive the relationship between the wetted section, perimeter, stage and depth. For two streams (Eggers Creek and Squaw Creek), we pinpointed inconsistencies in the topographic data, and we thus removed these data from the database. Authors employed non-metric units (feet and short tons), which we have thus converted into their metric counterparts. We also used the d_{50} and d_{90} values for the surface material provided by the authors. Bedload transport rates (reported in short ton per day) were measured using Helley-Smith samplers (with a 76.2-mm square entrance and a 0.25-mm mesh for the catch bag) (King, 2004).

Table S2. List of streams in Idaho and Nevada monitored by the Boise Adjudication Team and used in the review paper.

Name	Morphology	Slope (%)	d_{50} (mm)	Sample size	Measurement
Big Wood River	plane bed	0.91	119	100	Helley-Smith
Blackmare Creek	plane bed	2.99	95	88	Helley-Smith
Boise River	riffle-pool	0.38	76	82	Helley-Smith
Bruneau River	riffle-pool	0.54	41	66	Helley-Smith
Cat Spur Creek	riffle-pool	1.11	27	35	Helley-Smith
Dollar Creek	plane bed	1.46	87	85	Helley-Smith
Fourth of July	plane bed	2.02	51	78	Helley-Smith
Hawley Creek	plane bed	2.33	40	85	Helley-Smith
Herd Creek	plane bed	0.77	67	72	Helley-Smith
Jarbidge River	riffle-pool	1.6	95	56	Helley-Smith
Johns Creek	step-pool	2.07	207	115	Helley-Smith
Johnson Creek	plane bed	0.4	190	71	Helley-Smith
Little Buckhorn Creek	step-pool	5.09	81	77	Helley-Smith
Little Slate Creek	plane bed	2.68	102	157	Helley-Smith
Lochsa River	plane bed	0.23	148	72	Helley-Smith
Lolo Creek	plane bed	0.97	68	112	Helley-Smith
Main Fork Red River	plane bed	0.59	68	200	Helley-Smith
Marsch Creek	plane bed	0.6	56	98	Helley-Smith
Middle Fork Salmon River	plane bed	0.41	146	63	Helley-Smith
North Fork Clearwater River	plane bed	0.05	95	72	Helley-Smith
Rapid River	plane bed	0.19	96	61	Helley-Smith
Salmon River Below Yankee Fork	plane bed	0.34	104	60	Helley-Smith
Salmon River Near Obsidian	plane bed	0.66	61	50	Helley-Smith
Selway River	plane bed	0.21	173	72	Helley-Smith
South Fork Salmon River	plane bed	0.25	38	130	Helley-Smith
South Fork Payette River	plane bed	0.4	110	72	Helley-Smith
Thompson Creek	plane bed	1.53	59	81	Helley-Smith
Trapper Creek	step-pool	4.14	85	166	Helley-Smith
Valley Creek	plane bed	0.4	40	192	Helley-Smith
West Fork Buckhorn Creek	step-pool	3.2	180	85	Helley-Smith

S5.2 Gravel-bed rivers in the Rocky Mountains

We used the database proposed by the National Stream Aquatic Ecology Center (Bunte and Swingle, 2021). The database provided by Bunte and Swingle (2021) has similar features to the one made available by the Boise Adjudication Team. The only differences concern the measurement units (Bunte and Swingle (2021) used the metric system) and the d_{50} and d_{84} values for the surface material (rather than d_{90}).

Table S3. List of streams in the Rocky Mountains monitored by the National Stream Aquatic Ecology Center and used in the review paper.

Name	Morphology	Slope (%)	d_{50} (mm)	Sample size	Measurement
Barlow Creek	plane bed	2.4	62	31	Helley-Smith
Cache Creek	plane bed	2.1	46	60	Helley-Smith
Cherry Creek	plane bed	2.5	52	47	Helley-Smith
Clearwater River	plane bed	0.028	74	78	Helley-Smith
Coon Creek	plane bed	3.6	83	76	Helley-Smith
Deadhorse Creek	plane bed	2.9	50	59	Helley-Smith
East Dallas Creek	plane bed	1.7	60	60	Helley-Smith
East Fork Encampment River	plane bed	3.8	50	67	Helley-Smith
East Fork San Juan Creek	braiding	0.8	50	77	Helley-Smith
Florida Creek	plane bed	0.8	210	36	Helley-Smith
Fool Creek	plane bed	4.4	38	95	Helley-Smith
Halfmoon Creek	plane bed	1.06	64	133	Helley-Smith
Halfmoon Creek (riffle)	riffle-pool	1.55	56	176	Helley-Smith
Halfmoon Creek (bar)	bar	1.04	46	138	Helley-Smith
Hayden Creek	plane bed	2.5	63	78	Helley-Smith
Junction Creek	plane bed	2.8	50	34	Helley-Smith
Lexen Creek	step-pool	3.6	40	49	Helley-Smith
Little Granite Creek	plane bed	2.	89	96	Helley-Smith
Middle Fork Piedra River	plane bed	1.8	79	86	Helley-Smith
North Fork Swan Creek	plane bed	3.	39	62	Helley-Smith
Red Creek	plane bed	2.3	16	32	Helley-Smith
Saint Louis Creek site 1	step-pool	3.9	128	98	Helley-Smith
Saint Louis Creek site 2	plane bed	1.7	76	117	Helley-Smith
Saint Louis Creek site 3	plane bed	1.6	82	107	Helley-Smith
Saint Louis Creek site 4	plane bed	1.9	108	209	Helley-Smith
Saint Louis Creek site 4a	riffle-pool	1.9	80	189	Helley-Smith
Saint Louis Creek site 5	step-pool	4.8	140	93	Helley-Smith
Saint Louis Lower	plane bed	1.8	53	8	Helley-Smith
Saint Louis Upper	plane bed	1.8	75	18	Helley-Smith
Silver Creek	plane bed	4.5	28	57	Helley-Smith

S5.3 Other sources

We tried to find high-resolution bedload transport, but except for the data provided by Jonathan Laronne (Alexandrov et al., 2009; Cohen et al., 2010; Halfi et al., 2020) (for the Nahal Eshtemoa and Nahal Yatir, Israel), Ancey (2020) (for the Navisence, Switzerland), and Stark et al. (2021) (for the Arroyo de los Pinos, USA), our requests to access high-resolution were unsuccessful. High-resolution data are usually obtained using geophones and similar devices at high sampling rates (typically the integration time is one minute). For the data obtained on the Navisence (Ancey et al., 2014; Ancey, 2020), all bedload transport rates related to a give range of water discharge were collected and averaged, and thus Ancey (2020) provides ensemble-averaged transport rates. By contrast, Alexandrov et al. (2009), Cohen et al. (2010), Halfi et al. (2020), and Stark et al. (2021) provided data one ephemeral streams, collected during floods; integration times were 1 min or longer.

For the Caspar Creek (California, USA), we used the data available from
https://www.fs.usda.gov/rds/archive/catalog/RDS-2020-0017-2
provided by Richardson et al. (2020) and Richardson et al. (2021) collected at 10-min intervals during floods.

For the East Fork River (Wyoming, USA), we used the data provided by Emmett (1980), Emmett et al. (1980), Emmett et al. (1982), Leopold and Emmett (1976), Leopold and Emmett (1977), and Leopold and Emmett (1998). The amount of bedload trapped was weighted every minute. Only part of the data are provided and we do not know how the authors obtained the tabulated values from raw data.

For the Goodwin Creek (Mississippi, USA), we used the information provided by Kuhnle and Willis (1998) and the data recapped in (Almedeij, 2002).

For the Jacoby Creek (California, USA), data were obtained by Lisle (1986) and Lisle (1989). We used the data processed by Recking and available from his website:
https://www.bedloadweb.com

During her PhD thesis, Sirdari collected data on three sand-bed rivers in Malaysia (Sirdari, 2013; Sirdari et al., 2014). We used the data collected on the Kurau Rivier at 6 different places (including the confluence with the Ara River). Sampling duration ranged from 3 to 10 minutes.

We included the dataset collected by Jordan (1965) in the Mississippi River (USA) and made available by Brownlie (1981, 1985). Little information was given about the sampling procedure. Materials collected in the samplers whose size exceeded 0.125 mm was considered bedload.

As we did not have many bedload data related to sand river, we decided to include the data collected in the Mondego River (Portugal) by Da Cunha and made available by Brownlie (1981, 1985) although there is no information about the measurement procedure.

We used the data obtained by Einstein (1944) on the Mountain Creek (California, USA). Hydraulic conditions are missing, and we thus used the data post-processed by Brownlie (1981, 1985).

For the Oak Creek (Oregon, USA), we used the data collected by Milhous (1973) during his PhD thesis. Further information can also be found in (Laronne and Reid, 1993; Almedeij, 2002; Monsalve et al., 2020).

For the Riedbach River (Switzerland), we used the data collected by Schneider et al. (2016) during his PhD thesis.

We used the bedload transport data provided by Nordin and Beverage (1965) on the Rio Grande (New Mexico, USA). Like for the Mississippi River above, little information was given about the experimental protocol. Particles whose size exceeded 0.062 mm were considered bedload.

For the Sagehen Creek (California, USA), we used the data collected by Andrews (1994). The sampling duration was 4 min.

The torrent of Saint-Pierre (France) was studied by Meunier et al. (2006) and the data were made available by François Métivier from his homepage:
http://morpho.ipgp.fr/metivier/index
The sampling duration was 1 min.

For the Tordera River (Spain), general information can be found in (García et al., 2000). We used the data processed by Recking and available from his webpage (see the link to bedload.com above).

Similarly, for the Turkey Brook (UK), information is provided by Reid and Frostick (1986), and we used the data processed by Recking and available from his webpage (see the link to bedload.com above).

The Urumqi River (China) was monitored by a joint group from China and France (Liu et al., 2008, 2011; Guerit et al., 2014, 2018). We used the data processed by Métivier and available from his webpage (see the link to bedload.com above). Sampling duration was 120 s.

For the Versilia River (Italy), we used the information and data provided by Francalanci et al. (2013). Sampling duration was about 40 s.

Table S4. List of streams across the world whose data were used in our study. See the text for the references. The table only provides the mean features.

Name	Morphology	Slope (%)	d_{50} (mm)	Sample size	Measurement
Arroyo de los Pinos	plane bed	1.2	4	546	geophones
Caspar Creek	riffle-pool	1.4	17	1295	Birkbeck-style bedload pits
East Fork River	riffle-pool	0.07	1	140	bedload trap
Goodwin Creek	riffle-pool	0.24	12	358	Helley-Smith samplers
Jacoby Creek	riffle-pool	0.63	27	100	Helley-Smith samplers
Kurau	sand	0.35	1	48	Helley-Smith samplers
Mississipi	sand	0.005	0	165	P-46 samplers
Mondego	sand	0.080	2	219	?
Mountain Creek	sand	0.186	1	100	bedload traps
Nahal Yatir	riffle-pool	0.89	6	74	geophones
Nahal Eshtemoa	riffle-pool	0.75	16	682	geophones
Navisence	riffle-pool	3.2	80	120	geophones
Oak Creek	riffle-pool	0.95	54	119	Vortex VuV samplers
Riedbach (low slope)	riffle-pool	2.8	60	53	bedload traps
Rio Grande	sand	0.119	0	292	samplers
Sagehen Creek	riffle-pool	1.03	58	55	Helley-Smith samplers
Saint-Pierre	braiding	2.5	21	224	Helley-Smith samplers
Tordera	riffle-pool	2.	50	220	Birkbeck-type pit
Turkey Brook	riffle-pool	0.87	22	206	Birkbeck-type pit
Urumqi	braiding	2.5	20	194	Toutle-like samplers
Versilia	riffle-pool	0.2	22	11	Helley-Smith samplers

S6 Tables

All the data used in the paper are available in the form of Excel spreadsheets. All the Mathematica notebooks used for generating the figures in the review article and this electronic supplement are also available from `doi.org/10.5281/zenodo.7746863`.

S6.1 Scripts

These notebooks were tested under Mathematica 13.1. Some additional packages are required for the plots:

- the custom tick package library.wolfram.com/infocenter/MathSource/5599
- the MaTeX package library.wolfram.com/infocenter/MathSource/9355
- the quantile regression package (for Fig. 5 in the paper) resources.wolframcloud.com/FunctionRepository/r

Packages can be installed quickly with recent Mathematica versions (11.3 and later)

```
ResourceFunction[''MaTeXInstall''][]
```

See also how to install packages in mathematica
support.wolfram.com/5648?src=mathematica

Additional fonts to mimic the CM font in Mathematica are available from www.fontsquirrel.com/fonts/computer-modern

In the notebooks, it is possible to replace

```
FontFamily -> ''CMU Bright''
```

with

```
FontFamily -> ''Times New Roman''
```

S6.2 Field data

For the field-data spreadsheets "Data_USFD.xlsx", "Data_Bunte.xlsx", and "Data_other-sites.xlsx," we report the data described in § S5.1 (rivers in Idaho and Nevada), § S5.2 (rivers in the Rocky Mountains), and § S5.3 (other sites across the world), respectively. The variables used are the following ones:

- Name: river name
- Bedform: type of bedform
- slope: bed slope
- d50 [m]: median diameter
- d84 or d90 [m]: coarse grain diameter
- q [m^2·s^{-1}]: water discharge per unit width
- qs [m^2·s^{-1}]: bedload transport rate per unit width
- Rh [m]: hydraulics radius:
- shields: Shields number $\tau^* = \tau_b/(s\varrho g d_{50})$
- Phi: dimensionless transport rate $\Phi = q_s/\sqrt{sgd_{50}^3}$
- M: Martin's number $M = \Omega^{1/2}\xi^{-1/2}s^{-9/5}R^{-5/3}$

S6.3 Pipe and flume data

The spreadsheets "pipe-data.xlsx" and "flume-data.xlsx" include the following variables:

- Ref.: authors (year)
- case: run number
- type: type of facility
- W [m]: flow width
- slope: bed slope $i = \tan\theta$
- d_50 [m]: median diameter
- rho_s [kg·m^{-3}]: particle density ϱ_p/
- s [m]: density ratio $s = \varrho_p/\varrho - 1$
- q [m^2·s^{-1}]: water discharge per unit width
- qs [m^2·s^{-1}]: bedload transport rate per unit width
- h [m]: flow depth

- Rh [m]: hydraulic radius
- tau_b [Pa]: bottom shear stress $\tau_b = \varrho g R_h i$
- tau_b,corr [Pa]: corrected bottom shear stress
- f: bulk Darcy–Weisbach coefficient $f = 8giR_h/\bar{u}^2$ where $\bar{u} = q/h$ is the depth-averaged velocity
- f_b: bed Darcy–Weisbach coefficient
- e_b: efficiency factor computed as $e_b = q_s \mu \cos\theta g \Delta\varrho/\omega$
- e_b/mu: ratio of the efficiency factor to the bulk friction angle μ: $e_b/\mu = q_s \cos\theta g \Delta\varrho/\omega$
- Omega: scaled stream power $\Omega = \omega/(\nu g \varrho)$
- tau_*: Shields number $\tau^* = \tau_b/(s\varrho g d_{50})$
- Phi: dimensionless transport rate $\Phi = q_s/\sqrt{sgd_{50}^3}$
- M: Martin's number $M = \Omega^{3/2}\xi^{-1/2}s^{-9/5}R^{-5/3}$
- Π: dimensionless number $\Pi = \Omega^{1/2}\xi^{-1/2}s^{-4/5}R^{-2/3}$

The bottom shear stress is evaluated from the expression holding for steady uniform flow corrections

$$\tau_b = \varrho g R_h i, \tag{S59}$$

where R_h denotes the hydraulic radius and i is the bed slope. Sidewall friction may affect bottom shear stress. We use the method proposed by Johnson (1942). In particular, we solved Johnson's problem using the method developed by Guo (2017) by first determining wall friction through its Darcy–Weisbach coefficient f_w from the bulk Darcy–Weisbach coefficient $f = 8giR_h/\bar{u}^2$. This coefficient f_w is given by the equation

$$f_w = \frac{\ln^2 10}{36} \mathrm{W}^{-2} \left(\sqrt[3]{\frac{9\mathrm{Re}}{400 f}} \right) \tag{S60}$$

where Re denotes the Lambert W function and R is the flow Reynolds number

$$\mathrm{Re} = \frac{4R_h \bar{u}}{\nu},$$

with $\bar{u}$ the cross-section-averaged velocity. The bed Darcy–Weisbach friction is then obtained

$$f_b = \left(2\frac{h}{W} + 1\right) f - 2\frac{h}{W} f_w.$$

The corrected bed shear stress is then

$$\tau_{b,corr} = \frac{f_b}{8} \varrho \bar{u}^2.$$

References

Aberle, J. and Smart, G. M. (2003). The influence of roughness structure on flow resistance on steep slopes. *J. Hydraul. Res.*, 41:259–269.

Alam, A. M. Z. and Kennedy, J. F. (1969). Friction factors for flow in sand-bed channels. *J. Hydraul. Div. ASCE*, 95:1973–1992.

Alexandrov, Y., Cohen, H., Laronne, J. B., and Reid, I. (2009). Suspended sediment load, bed load, and dissolved load yields from a semiarid drainage basin: A 15-year study. *Water Resour. Res.*, 45(8).

Almedeij, J. H. (2002). *Bedload transport in gravel-bed streams under a wide range of Shields stresses.* PhD thesis, Virginia Polytechnic Institute and State University.

Ancey, C. (2020). Bedload transport: a walk between randomness and determinism. Part 2: Challenges and prospects. *J. Hydraul. Res.*, 58:18–33.

Ancey, C., Bohorquez, P., and Bardou, E. (2014). Sediment transport in mountain rivers. *Ercoftac*, 89:37–52.

Andrews, E. (1994). Marginal bed load transport in a gravel bed stream, Sagehen Creek, California. *Water Resour. Res.*, 30(7):2241–2250.

Armanini, A., Capart, H., Fraccarollo, L., and Larcher, M. (2005). Rheological stratification in experimental free-surface flows of granular-liquid mixtures. *J. Fluid Mech.*, 532:269–319.

Aziz, N. M. and Scott, D. E. (1989). Experiments on sediment transport in shallow flows in high gradient channels. *Hydrol. Sci. J.*, 34:465–478.

Bagnold, R. A. (1956). The flow of cohesionless grains in fluids. *Proc. R. Soc. London*, 249:235–296.

Bagnold, R. A. (1966). An approach to the sediment transport problem from general physics. Professional paper 422-I, United States Geological Survey.

Bagnold, R. A. (1980). An empirical correlation of bedload transport rates in flumes and natural rivers. *Proc. R. Soc. London ser. A*, 372:453–473.

Bagnold, R. A. (1986). Transport of solids by natural water flow: evidence for a worldwide correlation. *Proc. R. Soc. London ser. A*, 405:369–374.

Berzi, D. and Fraccarollo, L. (2013). Inclined, collisional sediment transport. *Phys. Fluids*, 25:106601.

Brownlie, W. R. (1981). Compilation of alluvial channel data: laboratory and field. Technical Report Report No. KH-R 43B, W. M. Keck Laboratory of Hydraulics and Water Resources, California Institute of Technology.

Brownlie, W. R. (1985). Compilation of alluvial channel data. *J. Hydraul. Eng.*, 111(7):1115–1119.

Bunte, K. and Swingle, K. W. (2021). Description and development of a database for bedload trap measurements in Rocky Mountain streams. Technical Report RMRS-GTR-420, US Department of Agriculture, Forest Service, Rocky Mountain Research Station.

Camenen, B., Bayram, A., and Larson, M. (2006). Equivalent roughness height for plane bed under steady flow. *J. Hydraul. Eng.*, 132:1146–1158.

Cao, H. H. (1985). *Résistance hydraulique d'un lit de gravier mobile à pente raide.* PhD thesis, Ecole Polytechnique Fédérale de Lausanne.

Capart, H. and Fraccarollo, L. (2011). Transport layer structure in intense bed-load. *Geophys. Res. Lett.*, 38:L20402.

Carling, P. (1989). Bedload transport in two gravel-bedded streams. *Earth Surf. Process. Landf.*, 14:27–39.

Cohen, H., Laronne, J. B., and Reid, I. (2010). Simplicity and complexity of bed load response during flash floods in a gravel bed ephemeral river: A 10 year field study. *Water Resour. Res.*, 46:W11542.

Colosimo, C., Copertino, V. A., and Veltri, M. (1988). Friction factor evaluation in gravel-bed rivers. *J. Hydraul. Eng.*, 114:861–876.

de Lange, S. I., Naqshband, S., and Hoitink, A. J. F. (2021). Quantifying hydraulic roughness from field data: can dune morphology tell the whole story? *Water Resour. Res.*, 57:e2021WR030329.

Deal, E. (2022). Flow resistance in very rough channels. *Water Resour. Res.*, 58:e2021WR031790.

Dey, S., Das, R., Gaudio, R., and Bose, S. K. (2012). Turbulence in mobile-bed streams. *Acta Geophys.*, 60:1547–1588.

Dey, S. and Raikar, R. V. (2007). Characteristics of loose rough boundary streams at near-threshold. *J. Hydraul. Eng.*, 133:288–304.

Einstein, H. A. (1944). Bed-load transportation in Mountain Creek. Technical Report SCS TP 55, Greenville Sediment Load Laboratory.

Einstein, H. A. (1950). The bed-load function for sediment transportation in open channel flows. Technical Report Technical Report No. 1026, United States Department of Agriculture.

Emmett, W. W. (1980). A field calibration of the sediment-trapping characteristics of the Helley-Smith bedload sampler. Technical report, US Government Printing Office.

Emmett, W. W., Myrick, R. M., and Meade, R. H. (1980). Field data describing the movement and storage of sediment in the East Fork River, Wyoming; Part I, River hydraulics and sediment transport, 1979. Report Open-File Report 80-1189, United States Geological Survey. TY - RPRT.

Emmett, W. W., Myrick, R. M., and Meade, R. H. (1982). Field data describing the movement and storage of sediment in the East Fork River, Wyoming; Part III, river hydraulics and sediment transport, 1980. Report 82-359. TY - RPRT.

Engelund, F. (1966). Hydraulic resistance of alluvial streams. *Journal of Hydraulic Division ASCE*, HY2:315–326.

Ferguson, R. I. (2007). Flow resistance equations for gravel- and boulder-bed streams. *Water Resour. Res.*, 43:W05427.

Ferguson, R. I. (2012). River channel slope, flow resistance, and gravel entrainment thresholds. *Water Resour. Res.*, 48:W05517.

Ferguson, R. I. (2021a). Limits to scale invariance in alluvial rivers. *Earth Surf. Process. Landf.*, 46:173–187.

Ferguson, R. I. (2021b). Roughness calibration to improve flow predictions in coarse-bed streams. *Water Resour. Res.*, 57:e2021WR029979.

Francalanci, S., Paris, E., and Solari, L. (2013). A combined field sampling modeling approach for computing sediment transport during flash floods in a gravel-bed stream. *Water Resour. Res.*, 49:6642–6655.

Gao, P. (2008). Transition between two bed-load transport regimes: Saltation and sheet flow. *J. Hydraul. Eng.*, 134:340–349.

García, C., Laronne, J. B., and Sala, M. (2000). Continuous monitoring of bedload flux in a mountain gravel-bed river. *Geomorphology*, 34:23–31.

Gaudio, R., Miglio, A., and Calomino, F. (2011). Friction factor and von Kármán's κ in open channels with bed-load. *J. Hydraul. Res.*, 49:239–247.

Gomez, B. (2006). The potential rate of bed-load transport. *Proc. Natl. Acad. Sci. U.S.A.*, 103:17170–17173.

Gomez, B. (2022). The efficiency of the river machine. *Geomorphology*, 410:108271.

Guerit, L., Barrier, L., Liu, Y., Narteau, C., Lajeunesse, E., Gayer, E., and Métivier, F. (2018). Uniform grain-size distribution in the active layer of a shallow, gravel-bedded, braided river (the Urumqi River, China) and implications for paleo-hydrology. *Earth Surf. Dyn,*, 6(4):1011–1021.

Guerit, L., Barrier, L., Narteau, C., Métivier, F., Liu, Y., Lajeunesse, E., Gayer, E., Meunier, P., Malverti, L., and Ye, B. (2014). The Grain-size Patchiness of Braided Gravel-Bed Streams—example of the Urumqi River (northeast Tian Shan, China). *Adv. Geosci.*, 37:27–39.

Guo, J. (2017). Exact procedure for Einstein–Johnson's sidewall correction in open channel flow. *J. Hydraul. Eng.*, 143:06016027.

Gust, G. and Southard, J. B. (1983). Effects of weak bed load on the universal law of the wall. *J. Geophys. Res. Oceans*, 88:5939–5952.

Guta, H., Hurther, D., and Chauchat, J. (2022). Bedload and Concentration Effects on Turbulent Suspension Properties in Heavy Particle Sheet Flows. *J. Hydraul. Eng.*, 148:04022012.

Halfi, E., Paz, D., Stark, K., Yogev, U., Reid, I., Dorman, M., and Laronne, J. B. (2020). Novel mass-aggregation-based calibration of an acoustic method of monitoring bedload flux by infrequent desert flash floods. *Earth Surf. Process. Landf.*, 45:3510–3524.

Hey, R. D. (1979). Flow resistance in gravel-bed rivers. *J. Hydraul. Div. ASCE*, 105:365–379.

Hohermuth, B. and Weitbrecht, V. (2018). Influence of bed-load transport on flow resistance of step-pool channels. *Water Resour. Res.*, 54:5567–5583.

Hsu, T. J., Jenkins, J. T., and Liu, P. L. F. (2004). On two-phase sediment transport: sheet flows of massive particles. *Proc. R. Soc. London ser. A*, 460:2223–2250.

Johnson, J. W. (1942). The importance of considering side-wall friction in bed-load investigations. *Civil Engineering*, 12:329–332.

Jordan, P. R. (1965). Fluvial sediment of the mississippi river at St. Louis, Missouri. Technical Report Water-Supply Paper 1802, United States Geological Survey.

Kamphuis, J. W. (1974). Determination of sand roughness for fixed beds. *J. Hydraul. Res.*, 12:193–203.

Keulegan, G. H. (1938). Laws of turbulent flows in open channels. *J. Res. Natl Bur. Stand.*, 21:707–741.

King, J. G. (2004). Sediment transport data and related information for selected coarse-bed streams and rivers in Idaho. Technical Report RMRS-GTR-131, US Department of Agriculture, Forest Service, Rocky Mountain Research Station.

Kuhnle, R. A. and Willis, J. C. (1998). Statistics of sediment transport in Goodwin Creek. *J. Hydraul. Eng.*, 124:1109–1114.

Lamb, M. P., Brun, F., and Fuller, B. M. (2017). Hydrodynamics of steep streams with planar coarse-grained beds: Turbulence, flow resistance, and implications for sediment transport. *Water Resour. Res.*, 53:2240–2263.

Laronne, J. B. and Reid, I. (1993). Very high rates of bedload sediment transport by ephemeral desert rivers. *Nature*, 366:148–150.

Leopold, L. B. and Emmett, W. W. (1976). Bedload measurements, East Fork River, Wyoming. *Proc. Natl. Acad. Sci. U.S.A.*, 73(4):1000–1004.

Leopold, L. B. and Emmett, W. W. (1977). 1976 bedload measurements, East Fork River, Wyoming. *Proc. Natl. Acad. Sci. U.S.A.*, 74(7):2644–2648.

Leopold, L. B. and Emmett, W. W. (1998). *Bedload and river hydraulics: inferences from the East Fork River, Wyoming.* US Department of the Interior, US Geological Survey.

Lisle, T. E. (1986). Stabilization of a gravel channel by large streamside obstructions and bedrock bends, Jacoby Creek, northwestern California. *Geol. Soc. Amer. Bull.*, 97(8):999–1011.

Lisle, T. E. (1989). Sediment transport and resulting deposition in spawning gravels, north coastal California. *Water Resour. Res.*, 25:1303–1319.

Liu, Y., Métivier, F., Gaillardet, J., Ye, B., Meunier, P., Narteau, C., Lajeunesse, E., Han, T., and Malverti, L. (2011). Erosion rates deduced from seasonal mass balance along the upper Urumqi River in Tianshan. *Solid Earth*, 2(2):283–301.

Liu, Y., Métivier, F., Lajeunesse, E., Lancien, P., Narteau, C., Ye, B., and Meunier, P. (2008). Measuring bedload in gravel-bed mountain rivers: averaging methods and sampling strategies. *Geodinamica Acta*, 21(1-2):81–92.

López, R. and Barragán, J. (2008). Equivalent roughness of gravel-bed rivers. *J. Hydraul. Eng.*, 134:847–851.

Manes, C., Pokrajac, D., and McEwan, I. (2007). Double-averaged open-channel flows with small relative submergence. *J. Hydraul. Eng.*, 133:896–904.

Martin, Y. and Church, M. (2000). Re-examination of Bagnold's empirical bedload formulae. *Earth Surf. Process. Landf.*, 25:1011–1024.

Matoušek, V. (2009). Concentration profiles and solids transport above stationary deposit in enclosed conduit. *J. Hydraul. Eng.*, 135:1101–1106.

Matoušek, V., Bareš, V., Krupička, J., Picek, T., and Zrostlík, v. (2016). Experimental evaluation of bed friction and solids transport in steep flume. *Can. J. Chem. Eng.*, 94:1076–1083.

Matoušek, V., Krupička, J., and Picek, T. (2013). Validation of transport and friction formulae for upper plane bed by experiments in rectangular pipe. *J. Hydrol. Hydromech.*, 61:120–125.

Maurin, R., Chauchat, J., and Frey, P. (2018). Revisiting slope influence in turbulent bedload transport: consequences for vertical flow structure and transport rate scaling. *J. Fluid Mech.*, 839:135–156.

Meunier, P., Métivier, F., Lajeunesse, E., Mériaux, A. S., and Faure, J. (2006). Flow pattern and sediment transport in a braided river: The "torrent de St Pierre" (French Alps). *J. Hydrol.*, 330(3):496–505.

Milhous, R. (1973). *Sediment transport in a gravel-bottomed stream.* PhD thesis, Oregon State University.

Millar, R. G. (1999). Grain and form resistance in gravel-bed rivers. *J. Hydraul. Res.*, 37:303–312.

Monsalve, A., Segura, C., Hucke, N., and Katz, S. (2020). A bed load transport equation based on the spatial distribution of shear stress—Oak Creek revisited. *Earth Surf. Dyn,*, 8:825–839.

Nikora, V. and Goring, D. (2000). Flow turbulence over fixed and weakly mobile gravel beds. *J. Hydraul. Eng.*, 126:679–690.

Nikora, V., Goring, D. G., McEwan, I., and Griffiths, G. (2001). Spatially averaged open-channel flow over rough bed. *J. Hydraul. Eng.*, 127:123.

Nikora, V., Koll, K., McEwan, I., McLean, S., and Dittrich, A. (2004). Velocity distribution in the roughness layer of rough-bed flows. *J. Hydraul. Eng.*, 130:1036–1042.

Nikora, V., McLean, S., Coleman, S., Pokrajac, D., McEwan, I., Campbell, L., Aberle, J., Clunie, D., and Koll, K. (2007). Double-averaging concept for rough-bed open-channel and overland flows: Applications. *J. Hydraul. Eng.*, 133:873–883.

Nikora, V. I., Stoesser, T., Cameron, S. M., Stewart, M. T., Papadopoulos, K., Ouro, P., McSherry, R., Zampiron, A., Marusic, I., and Falconer, R. A. (2019). Friction factor decomposition for rough-wall flows: theoretical background and application to open-channel flows. *J. Fluid Mech.*, 872:626–664.

Nnadi, F. N. and Wilson, K. C. (1992). Motion of contact-load particles at high shear stress. *J. Hydraul. Eng.*, 118:1670–1684.

Nordin, C. F. and Beverage, J. P. (1965). Sediment transport in the Rio Grande, New Mexico. Technical Report Professional Paper 462-F, US Geological Survey.

Omid, M. H., Karbasi, M., and Farhoudi, J. (2010). Effects of bed-load movement on flow resistance over bed forms. *Sadhana*, 35:681–691.

Pähtz, T. and Durán, O. (2020). Unification of aeolian and fluvial sediment transport rate from granular physics. *Phys. Rev. Lett.*, 124:168001.

Palucis, M. C., Ulizio, T. P., Fuller, B., and Lamb, M. P. (2018). Flow resistance, sediment transport, and bedform development in a steep gravel-bedded river flume. *Geomorphology*, 320:111–126.

Parker, C., Clifford, N. J., and Thorne, C. R. (2011). Understanding the influence of slope on the threshold of coarse grain motion: Revisiting critical stream power. *Geomorphology*, 126:51–65.

Parker, G. (1978). Self-formed rivers with equilibrium banks and mobile bed. Part 2. Gravel river. *J. Fluid Mech.*, 89:127–146.

Parker, G., Klingeman, P. C., and McLean, D. G. (1982). Bedload and size distribution in paved gravel-bed streams. *J. Hydraul. Div. ASCE*, 108:544–571.

Pazis, G. (1976). *Faible transport des sédiments par érosion et déposition dans les canaux alluvionnaires*. PhD thesis, École Polytechnique Fédérale de Lausanne.

Pitlick, J. (1992). Flow resistance under conditions of intense gravel transport. *Water Resour. Res.*, 28:891–903.

Pugh, F. J. and Wilson, K. C. (1999). Velocity and concentration distributions in sheet flow above plane beds. *J. Hydraul. Eng.*, 125:117–125.

Rebai, D., Berzi, D., Ballio, F., and Matousek, V. (2022). Experimental Comparison of Inclined Flows with and without Intense Sediment Transport: Flow Resistance and Surface Elevation. *J. Hydraul. Eng.*, 148:04022026.

Recking, A. (2006). *Experimental study of grain sorting effects on bedload*. PhD thesis, Institut National des Sciences Appliquées.

Recking, A. (2009). Theoretical development on the effects of changing flow hydraulics on incipient bed load motion. *Water Resour. Res.*, 45:W04401.

Recking, A., Frey, P., Paquier, A., Belleudy, P., and Champagne, J. Y. (2008a). Bed-load transport flume experiments on steep slopes. *J. Hydraul. Eng.*, 134:1302–1310.

Recking, A., Frey, P., Paquier, A., Belleudy, P., and Champagne, J. Y. (2008b). Feedback between bed load transport and flow resistance in gravel and cobble bed rivers. *Water Resour. Res.*, 44:W05412.

Redolfi, M., Tubino, M., Bertoldi, W., and Brasington, J. (2016). Analysis of reach-scale elevation distribution in braided rivers: Definition of a new morphologic indicator and estimation of mean quantities. *Water Resour. Res.*, 52:5951–5970.

Reid, I. and Frostick, L. E. (1986). Dynamics of bedload transport in Turkey Brook, a coarse-grained alluvial channel. *Earth Surf. Process. Landf.*, 11(2):143–155.

Revil-Baudard, T. and Chauchat, J. (2013). A two-phase model for sheet flow regime based on dense granular flow rheology. *J. Geophys. Res. Oceans*, 118:2012JC008306.

Richardson, P. W., Seehafer, J. E., Keppeler, E. T., Sutherland, D. G., Wagenbrenner, J. W., Bladon, K. D., Dymond, S. F., and Cole, R. P. (2021). Fifty-eight years and counting of watershed science at the Caspar Creek Experimental Watersheds in northern California. *Hydrolog. Process.*, 35(6):e14207.

Richardson, P. W., Wagenbrenner, J. W., Sutherland, D. G., and Lisle, T. E. (2020). Measuring and modeling gravel transport at Caspar Creek, CA, to detect changes in sediment supply, storage, and transport efficiency. *Water Resour. Res.*, 56(6):e2019WR026389.

Rickenmann, D. and Recking, A. (2011). Evaluation of flow resistance in gravel-bed rivers through a large field data set. *Water Resour. Res.*, 47:W07538.

Rouse, H. (1965). Critical analysis of open-channel resistance. *J. Hydraul. Div. ASCE*, 91:1–23.

Rousseau, G. and Ancey, C. (2022). An experimental investigation of turbulent free-surface flows over a steep permeable bed. *J. Fluid Mech.*, 941:A51.

Schneider, J. M., Rickenmann, D., Turowski, J. M., Schmid, B., and Kirchner, J. W. (2016). Bed load transport in a very steep mountain stream (Riedbach, Switzerland): Measurement and prediction. *Water Resour. Res.*, 52:9522–9541.

Sirdari, Z. Z. (2013). *Bedload transport of small rivers in Malaysia*. PhD thesis, University of Science Malaysia.

Sirdari, Z. Z., Ab Ghani, A., and Hassan, Z. A. (2014). Bedload transport of small rivers in Malaysia. *Int. J. Sediment Res.*, 29(4):481–490.

Song, T. (1994). *Velocity and turbulence distribution in non-uniform and unsteady open-channel flow*. PhD thesis, École Polytechnique Fédérale de Lausanne.

Song, T., Chiew, Y. M., and Chin, C. O. (1998). Effect of bed-load movement on flow friction factor. *J. Hydraul. Eng.*, 124:165–175.

Song, T., Graf, W. H., and Lemmin, U. (1994). Uniform flow in open channels with movable gravel bed. *J. Hydraul. Res.*, 32:861–876.

Stark, K., Cadol, D., Varyu, D., and Laronne, J. B. (2021). Direct, continuous measurements of ultra-high sediment fluxes in a sandy gravel-bed ephemeral river. *Geomorphology*, 382:107682.

Takahashi, T. (1981). Debris flow. *Annu. Rev. Fluid Mech.*, 13:57–77.

Thompson, S. M. and Campbell, P. L. (1979). Hydraulics of a large channel paved with boulders. *J. Hydraul. Res.*, 17:341–354.

van Rijn, L. (1984). Sediment transport, part III: bed forms and alluvial roughness. *J. Hydraul. Eng.*, 110:1733–1754.

Whiting, P. J., Stamm, J. F., Moog, D. B., and Orndorff, R. L. (1999). Sediment-transporting flows in headwater streams. *Geol. Soc. Amer. Bull.*, 111:450–466.

Wilson, K. C. (1966). Bed-load transport at high shear stress. *J. Hydraul. Div. ASCE*, 92:49–59.

Wilson, K. C. (1989). Mobile-bed friction at high shear stress. *J. Hydraul. Eng.*, 115(6):825–830.

Yager, E. M., Venditti, J. G., Smith, H. J., and Schmeeckle, M. W. (2019). The trouble with shear stress. *Geomorphology*, 323:41–50.